



**HAL**  
open science

## Scale-Dependent Kurtosis of Magnetic Field Fluctuations in the Solar Wind: A Multi-Scale Study With Cluster 2003-2015

O. W. Roberts, O. Alexandrova, L. Sorriso-Valvo, Z. Vörös, R. Nakamura, D. Fischer, A. Varsani, C. Philippe Escoubet, M. Volwerk, Patrick Canu, et al.

► **To cite this version:**

O. W. Roberts, O. Alexandrova, L. Sorriso-Valvo, Z. Vörös, R. Nakamura, et al.. Scale-Dependent Kurtosis of Magnetic Field Fluctuations in the Solar Wind: A Multi-Scale Study With Cluster 2003-2015. *Journal of Geophysical Research Space Physics*, 2022, 127, 10.1029/2021JA029483 . insu-03874885

**HAL Id: insu-03874885**

**<https://insu.hal.science/insu-03874885>**

Submitted on 11 May 2023

**HAL** is a multi-disciplinary open access archive for the deposit and dissemination of scientific research documents, whether they are published or not. The documents may come from teaching and research institutions in France or abroad, or from public or private research centers.

L'archive ouverte pluridisciplinaire **HAL**, est destinée au dépôt et à la diffusion de documents scientifiques de niveau recherche, publiés ou non, émanant des établissements d'enseignement et de recherche français ou étrangers, des laboratoires publics ou privés.

Copyright

# JGR Space Physics

## RESEARCH ARTICLE

10.1029/2021JA029483

### Special Section:

Cluster 20th anniversary: results from the first 3D mission

### Key Points:

- Multipoint Cluster magnetic field data (from 2003 to 2015) are used to investigate intermittency in solar wind plasma
- Two different methods are used to calculate fluctuations: temporal increments and spatial increments
- Spatial scales from  $\sim 10^1$  to  $\sim 10^4$  km are covered

### Correspondence to:

O. W. Roberts,  
[owen.roberts@oeaw.ac.at](mailto:owen.roberts@oeaw.ac.at)

### Citation:

Roberts, O. W., Alexandrova, O., Sorriso-Valvo, L., Vörös, Z., Nakamura, R., Fischer, D., et al. (2022). Scale-dependent Kurtosis of magnetic field fluctuations in the solar wind: A multi-scale study with Cluster 2003–2015. *Journal of Geophysical Research: Space Physics*, 127, e2021JA029483. <https://doi.org/10.1029/2021JA029483>

Received 24 APR 2021  
Accepted 26 AUG 2022

## Scale-Dependent Kurtosis of Magnetic Field Fluctuations in the Solar Wind: A Multi-Scale Study With Cluster 2003–2015

O. W. Roberts<sup>1</sup> , O. Alexandrova<sup>2</sup> , L. Sorriso-Valvo<sup>3,4</sup> , Z. Vörös<sup>1,5</sup> , R. Nakamura<sup>1</sup> , D. Fischer<sup>1</sup> , A. Varsani<sup>1</sup> , C. Philippe Escoubet<sup>6</sup> , M. Volwerk<sup>1</sup> , P. Canu<sup>7,8</sup> , S. Lion<sup>2</sup> , and K. Yearby<sup>9</sup> 

<sup>1</sup>Space Research Institute, Austrian Academy of Sciences, Graz, Austria, <sup>2</sup>Observatoire de Paris, LESIA, Université PSL, CNRS, Sorbonne Université, University Paris Diderot, Meudon, France, <sup>3</sup>Ångström Laboratory, Swedish Institute of Space Physics, Uppsala, Sweden, <sup>4</sup>Istituto per la Scienza e Tecnologia dei Plasmi (ISTP), Consiglio Nazionale delle Ricerche, Bari, Italy, <sup>5</sup>Institute of Earth Physics and Space Science, Eötvös Loránd Research Network, Sopron, Hungary, <sup>6</sup>ESA, European Space Research and Technology Centre, Noordwijk, The Netherlands, <sup>7</sup>LPP, CNRS, Ecole Polytechnique, Sorbonne Université, Palaiseau, France, <sup>8</sup>Observatoire de Paris, Université Paris-Saclay, PSL Research University, Paris, France, <sup>9</sup>Department of Automatic Control and Systems Engineering, University of Sheffield, Sheffield, UK

**Abstract** During the lifetime of the Cluster mission, the inter-spacecraft distances in the solar wind have changed from the large, fluid, scales ( $\sim 10^4$  km), down to the scales of protons ( $\sim 10^2$  km). As part of the guest investigator campaign, the mission achieved a formation where a pair of spacecraft were separated by  $\sim 7$  km. The small distances and the exceptional sensitivity of the search coil magnetometer provide an excellent data set for studying solar wind turbulence at electron scales. In this study, we investigate the intermittency of the magnetic field fluctuations in the slow solar wind. Using 20 time intervals with different constellation orientations of Cluster we cover spatial scales between 7 and  $10^4$  km. We compare time-lagged increments from a single spacecraft with spatially lagged increments using multiple spacecraft. As the turbulent cascade proceeds to smaller scales in the inertial range, the deviation from Gaussian statistics is observed to increase in both temporal and spatial increments in the components transverse to the mean field direction. At ion scales, there is a maximum of kurtosis, and at sub-ion scales, the fluctuations are only weakly non-Gaussian. In the compressive component the deviation from Gaussian statistics is variable: it may increase throughout the inertial and sub-ion ranges, but also, it may have a maximum at magnetohydrodynamic scales associated with large scale magnetic holes. The observations show differences in kurtosis of time and space increments when the spacecraft pairs are transverse to the flow, indicating its spatial anisotropy.

**Plain Language Summary** Turbulence in the slow solar wind is investigated using multi-spacecraft measurements for different satellites configurations. Twenty time intervals of more than 1 hr are analyzed. We compare differences in two time-delayed magnetic field measurements (time-lags) and of magnetic field measurements between spacecraft pairs (space-lags). Space-lags give the fluctuations along different satellite baseline directions and scales (from 7 to 9,000 km) while time-lags give the fluctuations along the flow direction. The magnetic field fluctuations' intermittency, which can be thought of as the “patchiness” or “roughness” is investigated. Differences are observed between the time-lagged measurements and the spatially lagged measurements when the spacecraft pairs are transverse to the flow.

## 1. Introduction

The solar wind is an excellent example of weakly compressive plasma turbulence (Bruno & Carbone, 2013). Compared to a neutral fluid, the physics is complicated by electromagnetic fields and various charged species with several different characteristic time and length scales. Existence of these scales result in several different distinct ranges where either fluid physics, proton kinetic, or electron kinetic physics dominate the dynamics of the plasma (Alexandrova, Chen, et al., 2013; Kiyani et al., 2015; Sahraoui et al., 2020; Verscharen et al., 2019, 2021).

The presence of a strong ambient magnetic field causes anisotropy to develop in the plasma (see the reviews of Horbury et al., 2005; Oughton et al., 2015). This gives rise to fluctuations that are organized around the mean magnetic field direction, with different properties along ( $\parallel$ ) and perpendicular ( $\perp$ ) to it. We distinguish (a) anisotropy of wavevectors  $k_{\parallel} \neq k_{\perp}$ , and (b) anisotropy of amplitude  $\delta B_{\parallel} \neq \delta B_{\perp}$  or power  $P_{\parallel} \neq P_{\perp}$  (Bieber et al., 1993, 1996; Chen, Horbury, et al., 2010; Chen, Wicks, et al., 2010; Horbury et al., 2008; Lacombe et al., 2017;

Mangeney et al., 2006; Matteini et al., 2020; Narita et al., 2011; Roberts et al., 2013; Sahraoui et al., 2010; Saur & Bieber, 1999; TenBarge et al., 2012). The relation between the two types of anisotropy was discussed in Chen, Wicks, et al. (2010), but it is not straightforward to assess using satellite data.

Turbulent fluctuations cover a broad inertial range of measured scales, ranging from the outer scale (typically equivalent to the auto-correlation time scale or to the scale of the  $1/f$  spectral break, when this is present, of the order of several hours) to the ion-kinetic-scale break (typically observed near 10 s at 1 AU). Within such a range, the definition of a mean field direction is a delicate issue. As a result of the various time and length scales, the plasma dynamics may be related to a local (temporally or spatially limited) magnetic field (Chen et al., 2012; Horbury et al., 2008; Kiyani et al., 2013), rather than a global mean over the chosen time interval.

Intermittency, one of the key properties of turbulence, indicates the scale-dependent inhomogeneity of the energy cascade and dissipation (Bruno, 2019; Frisch, 1995; Kolmogorov, 1962; Matthaeus et al., 2015). It is observed as the scale dependence of the probability distribution function (PDF) of turbulent fluctuations (Sorriso-Valvo et al., 1999), which in standard models describes a deviation from self-similar or monofractal scaling (e.g., Carbone et al., 2018; Chen, Leung, et al., 2014; Chen, Sorriso-Valvo, et al., 2014; Chhiber et al., 2021; Kiyani et al., 2009; Macek, 2007; Macek et al., 2011; Mangeney et al., 2001; Roberts, Thwaites, et al., 2020; Salem et al., 2009). Intermittency is associated with the development of coherent structures. These are termed coherent structures as they exhibit phase coherence over many scales simultaneously (Frisch, 1995; Hada et al., 2003; Koga & Hada, 2003; Lion et al., 2016; Mangeney et al., 2001; Perri, Carbone, et al., 2012; Perrone et al., 2017; Veltri, 1999). Some examples include current sheets (e.g., Borovsky & Podesta, 2015; Perri, Goldstein, et al., 2012), Alfvénic vortices (Alexandrova, 2008; Alexandrova et al., 2006; Alexandrova & Saur, 2008; Lion et al., 2016; Perrone et al., 2017; Roberts et al., 2013, 2016; Wang et al., 2019), or flux ropes (Vörös et al., 2016). These examples are predominantly incompressible structures characterized by  $\delta B_{\perp} \gg \delta B_{\parallel}$ . However, there are structures such as magnetic holes (Génot, 2008; Génot et al., 2009; Soucek & Escoubet, 2011; Soucek et al., 2008; Volwerk et al., 2020, 2021), vortices, shocks or solitons that have large variations in the compressive component such that  $\delta B_{\parallel} \gg \delta B_{\perp}$  or  $\delta B_{\parallel} \simeq \delta B_{\perp}$  depending on the structure type (Jovanović et al., 2020; Perrone et al., 2016). As coherent structures have a particular orientation along mean field, they are localized in space and have different variance anisotropy. The intermittency properties are observed to be anisotropic in terms of variance (Bruno et al., 2003; Perri et al., 2009; Sorriso-Valvo et al., 2006, 2010) and wavevectors (Chasapis et al., 2020; Yordanova et al., 2015).

It is common to define turbulent fluctuations as time delayed increments at a given scale. Thus, we define magnetic field fluctuations at timescale  $\tau$  as:

$$\delta \mathbf{B}(t, \tau) = \mathbf{B}(t + \tau) - \mathbf{B}(t). \quad (1)$$

The probability distribution functions (PDFs) of  $\delta B(t, \tau)$  at large scales ( $\tau \simeq 24$  hr) are usually close to a Gaussian distribution, but they become increasingly high-tailed as the turbulent cascade proceeds to smaller scales ( $\tau$  of few seconds), (e.g., Bruno et al., 2004; Sorriso-Valvo et al., 1999). The intermittency level can be quantified by investigating the anomalous scaling of the higher-order moments of these PDFs. One important example is the timescale dependence of the kurtosis, defined for the  $i$ th component of the magnetic field as:

$$K_i(\tau) = \frac{\langle \delta B_i^4(t, \tau) \rangle_t}{\langle \delta B_i^2(t, \tau) \rangle_t^2}, \quad (2)$$

where the angled brackets  $\langle \dots \rangle_t$  indicate ensemble (time series) average. The kurtosis is a measure of how heavy the tails of the PDFs are, quantifying the deviation from a Gaussian distribution, which has a kurtosis of 3. Larger values indicate heavier tails of the distribution, caused by rare, large-amplitude fluctuations associated with coherent structures. Large gradients in the magnetic field fluctuations have been observed simultaneously with enhancements in plasma heating in both numerical simulations and spacecraft data (Chasapis, Matthaeus, Parashar, Fuselier, et al., 2017; Chasapis, Matthaeus, Parashar, LeContel, et al., 2017; Osman et al., 2011; Sorriso-Valvo et al., 2018; Wu et al., 2013; Yordanova et al., 2021). Therefore, understanding the role of coherent structures is essential to quantify the turbulent heating present in the solar wind.

At scales smaller than the proton gyroradius, the intermittency properties are unclear, and there are conflicting results. In several solar wind studies (Carbone et al., 2018; Chasapis, Matthaeus, Parashar, Fuselier, et al., 2017; Chasapis, Matthaeus, Parashar, LeContel, et al., 2017; Chen, Leung, et al., 2014; Chen, Sorriso-Valvo,

et al., 2014; Chhiber et al., 2018, 2021; Kiyani et al., 2009, 2013; Roberts, Thwaites, et al., 2020) the fluctuations in magnetic and density measurements have been shown to exhibit self-similar, monofractal behavior, which is associated with constant kurtosis. It should be noted that for a measurement of kurtosis (or other higher order moments) the uncertainty can be large as they are very sensitive to rare fluctuations which may be poorly sampled in a finite signal. To mitigate these effects the largest fluctuations can be removed from the calculation (e.g., Kiyani et al., 2006) so that the error in the moments is reduced. The mono-fractal scaling in the sub-ion scale contrasted starkly with multifractal behavior seen at magnetohydrodynamic (MHD) scales (Kiyani et al., 2009). The interpretation of these observations is not clear. The nature of turbulent fluctuations changes at ion scales and the non-linear time of interaction changes as well. At these scales, the current sheets built-up through the MHD cascade (e.g., Boldyrev, 2006; Borovsky & Podesta, 2015; Chandran et al., 2015; Mallet et al., 2011), can break-up via reconnection (Vech et al., 2018), creating small-scale flux ropes or vortices (Mallet et al., 2011), thus changing the topology of the dominant intermittent events. A drop in the kurtosis near ion scales may be related to stochastic heating (e.g., Mallet et al., 2019). Reconnection can also excite waves at ion and electron scales (Alexandrova et al., 2016; Khotyaintsev et al., 2019). Moreover, as a function of ion temperature anisotropy, kinetic plasma instabilities (e.g., Hellinger et al., 2006; Hellinger & Travnicek, 2008; Klein et al., 2018) may superimpose to the cascade (Alexandrova, Chen, et al., 2013) and excite waves at ion scales. These waves could mix up phases of turbulent fluctuations and thus reduce kurtosis at sub-ion scales. On the other hand, in the planetary magnetosheaths, the increase of kurtosis of magnetic field fluctuations even at sub-ion scales is observed, suggesting intermittency (e.g., Alberti et al., 2021; Bowen et al., 2020; Chhiber et al., 2018; Huang, Schmitt, et al., 2021; Huang, Xiong, et al., 2021; Tao et al., 2015; von Papen et al., 2014).

The constant or even decreasing scale-dependent kurtosis often observed in the solar wind could be due to instrumental noise in the magnetic field measurements as the amplitudes of fluctuations are much smaller than in the magnetosheath, (e.g., Chhiber et al., 2018). However, observations with higher signal-to-noise ratios (SNRs) than the solar wind interval of Chhiber et al. (2018) have also shown a plateau in the kurtosis (i.e., monofractal scaling) at sub-ion scales in the solar wind (Chen, Leung, et al., 2014; Chen, Sorriso-Valvo, et al., 2014; Chhiber et al., 2021; Roberts, Thwaites, et al., 2020; Roberts, Verscharen, et al., 2020) in planetary magnetosheaths, (Hadid et al., 2015; Quijia et al., 2021), in numerical simulations (Cerri et al., 2019; Wu et al., 2013) and laboratory plasmas (Schaffner & Brown, 2015).

Finally, using single-point density measurements Sorriso-Valvo et al. (2017) found that even for the same interval, various analysis methods (multifractal spectra, anomalous scaling of structure-function exponents, and the scaling properties of the kurtosis) may yield different conclusions, suggesting that different methods capture different properties of intermittency.

The goal of this paper is to further investigate the intermittency in solar-wind magnetic-field fluctuations. Most studies focus on single-spacecraft measurements, where a time lag is used to obtain the fluctuation at different scales, Equation 1. Assuming the validity of Taylor's frozen-in flow hypothesis, one may convert a time lag  $\tau$  to a spatial lag  $\lambda_{\text{stream}} = \tau V_{\text{sw}}$  along the stream direction. This allows the study of different spatial scales along the bulk flow direction.

In order to investigate the wavevector anisotropy of turbulence with respect to the mean magnetic field  $B_0$ , measurements must be taken along and perpendicular to the field at the same time. This is not always possible with the present instrumentation. Most works on this subject have been done by assuming that measurements taken at different times but with different angle of the bulk speed with respect to  $B_0$ ,  $\theta_{\text{BV}}$ , will be representative statistically (see, e.g., Horbury et al., 2008; Wang et al., 2020; Zhang et al., 2022). Here we propose to use Cluster satellites to complete the view along the bulk flow by measurements between different satellites oriented differently to the bulk flow and to the magnetic field.

When a fluctuation is measured by two spacecraft,  $C_i$  and  $C_j$ , at position vectors  $\lambda_i, \lambda_j$  (at the same time  $t$ ), separated by  $\lambda = \lambda_i - \lambda_j$ , a spatially lagged increment can be defined as

$$\delta \mathbf{B}(\mathbf{t}, \lambda) = \mathbf{B}(t, \lambda_i) - \mathbf{B}(t, \lambda_j). \quad (3)$$

Thus, we define the kurtosis as a function of spatial scale  $\lambda$  as

$$K_i(\lambda) = \frac{\langle \delta B_i^4(t, \lambda) \rangle_t}{\langle \delta B_i^2(t, \lambda) \rangle_t^2}. \quad (4)$$

Below, we will use the notation  $\lambda_{\text{baseline}}$  for  $\lambda$  to underline the fact that the spatial lags calculated using two satellites give a measurement of the spatial scale along the satellites baseline direction.

To investigate both the scale and directional dependence it is preferable to have many baselines at various scales sampling the same plasma in many different directions at the same time (Dai et al., 2020; Klein et al., 2019; Matthaeus et al., 2019; Montgomery, 1980; Schwartz et al., 2011). However, this is not currently possible. An alternative is to investigate numerous intervals, similar in terms of their plasma parameters where the spacecraft separations and orientations vary. This approach also has the limitation that the different samples are not from the same plasma. For example, there could be subtle differences due to the solar cycle (Chapman et al., 2008), or slow solar wind can in some cases have similar Alfvénicity as fast wind (D'Amicis et al., 2018). In the current absence of any alternative, this approach is pursued here. A similar study was performed with Magnetospheric Multiscale's (MMS) fluxgate magnetometer by Chasapis, Matthaeus, Parashar, Fuselier, et al. (2017), Chasapis, Matthaeus, Parashar, LeContel, et al. (2017). However, as previously mentioned, the sensitivity of MMS' magnetic field instruments are not sufficient to study electron scale physics in the solar wind. In the frequency range  $f_{\text{sc}} > 1$  Hz, in the solar wind at 1 astronomical unit the search-coil magnetometer on Cluster has the best sensitivity, (e.g., Hospodarsky, 2016). In this work, we will use data from the many years that Cluster has been active to study a larger number of intervals where the inter-spacecraft distances span from  $10^4$  km down to 7 km.

## 2. Data and Methodology

Over the last 20 years, the Cluster mission (Escoubet et al., 1997, 2001) has provided multi-point data of the solar wind with a variety of spacecraft baseline lengths and constellation geometries. In 2015 the distance between spacecraft C3 and C4 was reduced to a few kilometers, and several intervals of burst mode data in the solar wind were measured as part of the Cluster guest investigator (GI) program (For further details of the GI program the reader is referred to <http://sci.esa.int/cluster/55616-guest-investigator-operations-2015-2016/>). In this study, magnetic field data are used from multiple spacecraft.

Table 1 gives the list of the selected intervals in the slow solar wind, which is generally more abundant in the Cluster data set. The choice of data excludes fast wind and interaction regions as their intermittency properties can be different (Bruno et al., 2003; Sorriso-Valvo et al., 1999). We attempt to have similar values for many of the parameters, however we cannot ensure homogeneity between intervals. In a strict sense, to obtain homogeneity and to be able to compare many spatial lags with one another the same plasma must be sampled by a large number of sampling points. The sampling points would ideally have a variety of baseline distances and angles with respect to the magnetic field. Variations in the plasma  $\beta$  and the angle  $\theta_{\text{BV}}$  can also affect the results. As one can see from Table 1, the ion and electron plasma  $\beta$  (the ratio of thermal to magnetic pressures) are within the limits of 0.3–2.0. To calculate  $\beta_{i,e}$  we use the electron density  $n_e$  from the plasma electron and current experiment (PEACE), (Johnstone et al., 1997). The electron temperature  $T_e$  also comes from PEACE, while Cluster ion spectrometry's (CIS) hot ion analyzer (HIA) (Reme et al., 1997, 2001) gives  $T_i$ . When HIA is unavailable the measurement from COmposition and DIstribution Function (CODIF) is used.

A magnetic connection to the terrestrial foreshock could result in the presence of foreshock whistlers and more complex waves with shorter correlation lengths that would not be characteristic of the pristine solar wind (e.g., Alexandrova, Bale, & Lacombe, 2013; Turc et al., 2019). Therefore, we visually check the spectra from CIS to ensure that there are no high-energy backstreaming particles and that the electric-field spectrogram is quiet, so that a connection is unlikely or of very short duration compared to the interval size.

The DC magnetic field on Cluster is measured by the fluxgate magnetometers (FGM) (Balogh et al., 2001), which have a sampling rate of 22.416 Hz in normal mode, and 67.249 Hz in burst mode. The digitization error on FGM data is 0.008 nT (Balogh et al., 2001). Thus, in the solar wind, the FGM measurements can typically be used up until about 1–2 Hz. At higher frequencies, FGM sensitivity is not sufficient. We will use the FGM data to study MHD range fluctuations, that is,  $f < 1$  Hz and  $\lambda_{ij} > 140$  km.

To cover kinetic scales, we use the spatio temporal analysis of field fluctuations (STAFF-SC) instrument (Cornilleau-Wehrin et al., 1997, 2003). STAFF-SC is a search coil magnetometer, which measures the AC magnetic field. It has a sampling rate of 25 Hz in normal mode and 450 Hz (a Nyquist frequency of 225 Hz) in burst mode. The burst mode STAFF-SC data provided on the Cluster science archive (Laakso et al., 2010) are filtered such that only frequencies between 0.6 and 180 Hz are present in the spectrum, avoiding the presence of

**Table 1**  
*List of Intervals Analyzed in This Study*

Int	Date	Start	End	$B_0$	$v_{sw}$	$\beta_i$	$\beta_e$	Max $ \lambda $	Min $ \lambda $	$\rho_i$	$\rho_e$
1	2003-02-10	18:00:00	22:00:00	7.1	435.	1.0	0.7	3,843.	3,504.	73.7	1.7
2	2003-02-11	12:40:00	14:00:00	7.1	422.	0.8	0.7	10,563.	3,743.	90.4	1.6
3	2003-02-25	13:30:00	15:30:00	6.4	401.	0.9	0.8	8,220.	2,766.	71.9	1.7
4	2003-03-11	09:00:00	11:00:00	7.8	419.	1.0	1.0	3,976.	3,351.	69.3	1.7
5	2004-02-09	12:30:00	15:30:00	5.7	408.	1.0	0.6	250.	171.	91.8	2.1
6	2004-02-21	17:00:00	20:30:00	8.0	382.	0.8	0.9	233.	146.	56.5	1.7
7	2004-03-06	16:00:00	16:40:00	5.1	373.	0.8	1.0	261.	176.	77.8	2.2
8	2005-02-21	18:00:00	19:30:00	4.7	397.	1.0	0.5	1,098.	879.	115.1	2.3
9	2005-03-24	04:00:00	07:00:00	6.8	310.	0.9	1.0	1,279.	830.	48.6	1.7
10	2006-02-02	12:10:00	14:00:00	6.3	343.	0.9	1.6	13,458.	5,291.	69.9	2.4
11	2006-02-28	08:00:00	11:00:00	6.8	349.	0.6	1.4	13,872.	5,207.	61.2	2.4
12	2006-04-04	18:00:00	22:00:00	7.8	317.	0.5	0.8	13,231.	5,779.	39.4	1.4
13	2007-01-27	05:10:00	07:40:00	4.1	300.	1.1	2.0	13,238.	428.	79.8	2.7
14	2007-02-05	14:30:00	18:00:00	5.0	337.	1.0	1.3	12,851.	485.	77.2	2.4
15	2007-02-08	18:40:00	20:30:00	4.5	443.	1.3	1.1	11,433.	399.	140.3	2.9
16	2010-02-09	22:00:00	23:00:00	5.9	306.	0.4	0.3	11,786.	201.	56.7	1.7
17	2012-02-04	03:00:00	03:59:30	6.8	449.	NA (0.3)	0.5	7,167.	53.	NA (57)	1.7
18	2012-02-22	04:30:00	05:30:00	5.7	421.	NA (0.6)	2.1	6,798.	117.	NA (42)	2.0
19	2015-02-11	09:50:00	10:10:00	6.3	469.	NA (0.4)	0.7	9,405.	6.	NA (50)	2.1
20	2015-02-15	21:25:00	22:40:00	9.3	336.	0.8	0.5	9,653.	7.	86.6	1.2

*Note.* Times are indicated in Universal Time, mean magnetic field over the interval,  $B_0$ , is given in nT, the ion bulk velocity measured by Cluster Ion Spectrometer (CIS) is given in km/s,  $\beta$  is the dimensionless ratio of the thermal to magnetic pressure (with  $i$  and  $e$  referring to ion and electrons, PEACE electron density is used for calculation of  $\beta_{i,e}$ ),  $|\lambda|$  is the magnitude of the separation vector between two spacecraft with the minimum/maximum separations shown in km,  $\rho_{i,e}$  denote the ion and electron Larmor radii in km/rad calculated from CIS and PEACE respectively. If CIS is not available, then the electron velocity from PEACE is used for the bulk velocity, and data from OMNI King and Papitashvili (2005) is used for  $\beta_i$  and  $\rho_i$ , which are indicated in round brackets.

spin tones at 0.25 and 0.5 Hz. The time resolution in burst mode is 0.0022 s, and is enough to avoid any blurring effect (Bandyopadhyay et al., 2018) at the smallest satellites separations of 6–7 km, where the advection time between the satellites (if flow-aligned) is about  $\Delta t = 0.013$  s for a reasonable upper bound of the bulk speed of the slow wind  $V_{sw} = 450$  km/s. For two spacecraft that are separated transversely to the bulk velocity, there is no blurring effect as they measure different cuts through the plasma and there is no advection between points.

Attention must be paid to the sensitivity of STAFF-SC instrument, which is frequency-dependent. The sensitivity level has been estimated on ground (Cornilleau-Wehrin et al., 1997) and then verified in-flight using magnetospheric lobes measurements (Alexandrova et al., 2010; Kiyani et al., 2013; Robert et al., 2014). Table A1 in Appendix A gives examples of the STAFF-SC errors on C3 and C4 at different frequencies. We see that STAFF-SC is more sensitive at higher frequencies than FGM and thus more appropriate for the study of sub-ion scale magnetic fluctuations. See Appendix A for more details on the STAFF-SC sensitivity and also Appendix B for a detailed discussion of the STAFF sensitivity on spatial and temporal lags.

To have a time series which covers turbulent fluctuations at all scales, from MHD to electron scales, we merge FGM and STAFF-SC measurements. Merging can be done in several different ways (e.g., Alexandrova et al., 2004; Argall et al., 2018; Bowen et al., 2020; Chen, Horbury, et al., 2010; Chen, Wicks, et al., 2010; Fischer et al., 2016; Kiyani et al., 2009). In this work, we elect to merge the data using a procedure based on what has been used for merging data on the Magnetospheric MultiScale Mission (Argall et al., 2018; Fischer et al., 2016). The data (both FGM and STAFF-SC) are interpolated onto a regular time grid with the time resolution of the STAFF-SC data.

The FGM data is filtered with a sinc function at around 0.6–1 Hz to remove the high-frequency part, where FGM is not sensitive. The STAFF-SC data are high-pass filtered at 0.6 Hz, as discussed above. The exact filtering frequency for FGM data varies with the magnetic field component as they have slightly different noise floors and signal powers in the STAFF-SC data. Precisely, we apply the low-pass filter at [0.98, 1.41, 1.52] Hz frequencies for  $B_x$ ,  $B_y$ , and  $B_z$  components of FGM, respectively. Then, signals on two instruments are added in the time domain. Some excess (or reduced) power may be introduced near the frequencies where the merging is done. This will slightly affect time lags near the merging frequency. For the spatial lags at small scales we use the STAFF-SC data, and the merged data are only used for mean field determination. Indeed, if we calculate spatial increments, Equation 3, at small scales with merged data, large-scale fluctuations appear due the independent noise at all frequencies on two spacecraft, see Appendix B for more details.

A final consideration related to the data quality is the time synchronization between two spacecraft. The STAFF-SC data on the Cluster Science Archive (Laakso et al., 2010) contains an additional timing correction (Yearby et al., 2013). This correction ensures that the difference in the timing synchronization between spacecraft is smaller than 20  $\mu$ s, as quoted in the STAFF calibration report, and will not affect the analysis. It is important to note that the time corrections are not applied to the fluxgate magnetometer data. However, as the DC magnetic-field data are only used up until  $\sim$ 2 Hz, an error in the time tags is unlikely to be significant. Thus, we can resample the FGM data onto a regular time grid with the same time resolution as the STAFF-SC data.

The time and space increments will be analyzed in a coordinate system related to a mean magnetic field. Indeed, the definition of a mean field is a delicate issue in the solar wind. The “global” mean coordinate system can be used when the magnetic field direction is relatively constant within the time interval. If the ambient field direction changes significantly during the interval, a typical situation in the non-stationary solar wind (e.g., Jagarlamudi et al., 2019), the global coordinate system can be flawed.

To overcome this problem, we can define a “local” or scale-dependent magnetic field direction, which are either based on wavelet analysis (e.g., He et al., 2011; Horbury et al., 2008; Kiyani et al., 2013) or on the mean between spatially or temporally separated points (e.g., Chen et al., 2012; Wang et al., 2020). For a fluctuation across a specific timescale  $\tau$  (or spatial scale  $\lambda$ ), a local mean magnetic field direction can be defined as

$$\mathbf{B}_{\text{local}}(t, \tau) = [\mathbf{B}(t) + \mathbf{B}(t + \tau)]/2 \quad (5)$$

for a time lag, or

$$\mathbf{B}_{\text{local}}(t, \lambda) = [\mathbf{B}(t, \lambda_i) + \mathbf{B}(t, \lambda_j)] / 2 \quad (6)$$

for a spatial lag  $\lambda = \lambda_i - \lambda_j$ . The two perpendicular directions can be defined as

$$\mathbf{e}_{\perp 1} = \frac{\mathbf{B}_{\text{local}} \times \mathbf{V}_{sw}}{|\mathbf{B}_{\text{local}} \times \mathbf{V}_{sw}|} \quad (7)$$

and

$$\mathbf{e}_{\perp 2} = \hat{\mathbf{B}}_{\text{local}} \times \mathbf{e}_{\perp 1} \quad (8)$$

respectively, where the hat denotes the unit vector.

A local magnetic field follows the field direction so closely that the gradients usually observed in the global mean field coordinate system do not appear anymore (Roberts, Thwaites, et al., 2020). Note, however, that the local average is itself a turbulent quantity that will have scale-dependent statistics. This can entangle with the scale-dependent statistics of the field, which may affect the analysis results (see e.g., Oughton & Matthaeus, 2020). Some caution is therefore necessary when comparing data analysis based on the local mean-field to predictions from models of turbulence. In this paper, since we do not make any explicit reference to turbulence models but only comparatively quantify deviation from Gaussian statistics, the above issues are expected to be irrelevant.

### 3. Results

#### 3.1. Cluster GI Interval on the 15th of February 2015

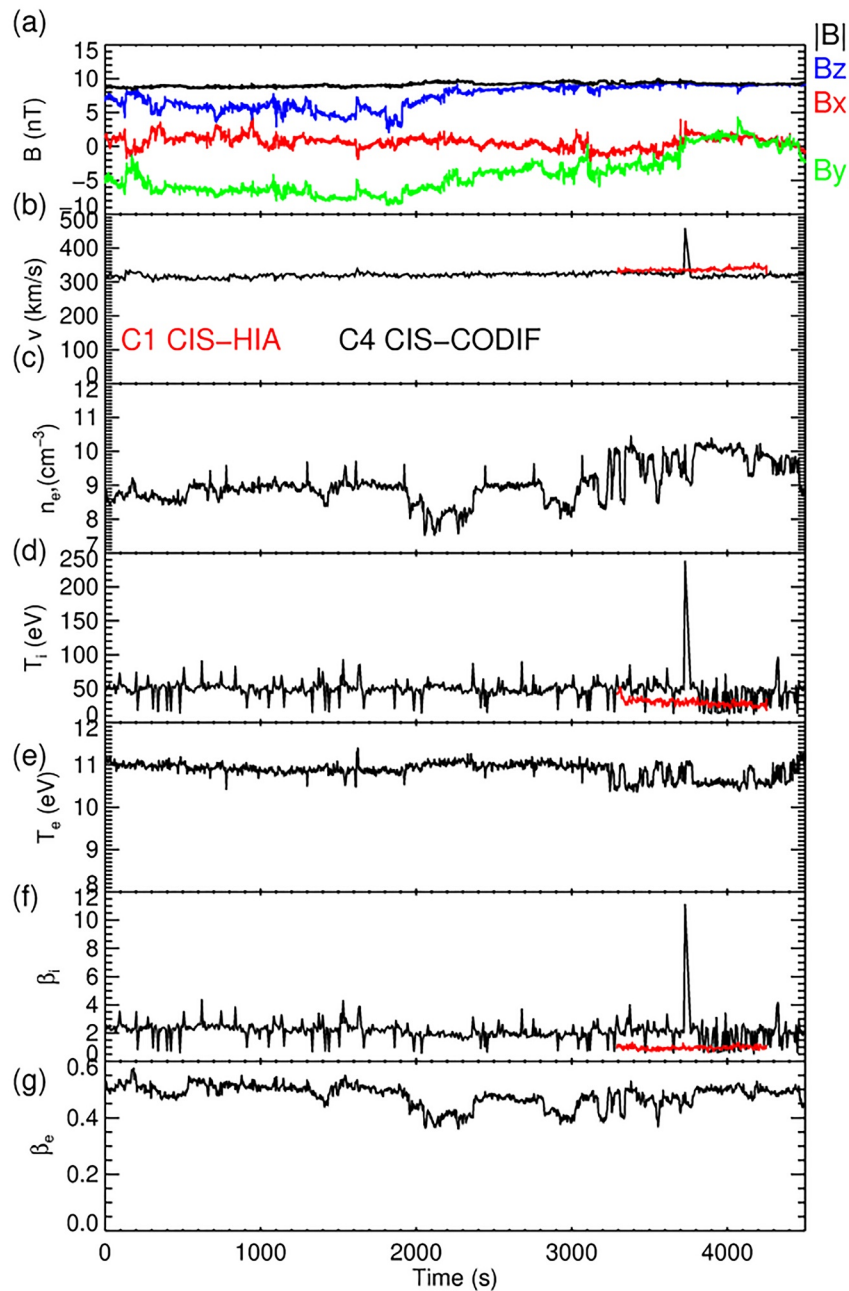
We perform an in-depth study of one of these selected intervals from the GI program, which occurs between 21:25–22:40 UT on the 15th of February 2015 (denoted interval 20 in Table 1). This interval was chosen because it is one of the longest intervals during this GI campaign of continuous pristine solar wind without excursions to the bow shock.

Figure 1 shows an overview of the interval, where the magnetic field from the fluxgate magnetometer (a), the bulk speed data (b), and ion temperature (d) from the CIS- CODIF and the HIA (Reme et al., 1997, 2001) are displayed. Electron density and temperature from PEACE (Johnstone et al., 1997) are shown in panels (c) and (e). Finally, the ion and electron plasma  $\beta$  are shown in panels (f) and (g). There is an anomaly in HIA for most of this interval where the counts and the velocity become very low. Between 22:05 UT and 22:35 UT, the instrument operates normally, as shown by red line in Figures 1b, 1d, and 1f. In burst mode, HIA operates for an hour. However, it takes some time for the instrument to switch on and off, resulting in anomalous counts. The CODIF, PEACE, and HIA instruments (when it is not having anomalous counts) agree with ion and electron velocities having similar values  $V_{sw} \simeq 335$  km/s. This estimate of the bulk speed is also confirmed from OMNI data (King & Papitashvili, 2005) at the same time.

During this interval, the spacecraft C3 and C4 are separated by 7 km. The baselines made with the other spacecraft range between 4,000 and 9,000 km and do not vary significantly throughout the interval. The mean and standard deviations of the baseline magnitudes are  $[\lambda_{12}, \lambda_{13}, \lambda_{14}, \lambda_{23}, \lambda_{24}, \lambda_{34}] = [4,000 \pm 100, 6,650 \pm 60, 6,700 \pm 60, 9,600 \pm 200, 9,600 \pm 200, 6.61 \pm 0.04]$ . Note that the differences between the baselines made with C3 and C1, C2 are very similar to those made with C4 and C1, C2, because C3 and C4 are so close to one another. Figure 2, left panels, gives the configurations of all Cluster spacecraft with more detail on C3 and C4's relative positions in the right panels. The satellites separations are shown in the global mean field measured from C4 and bulk flow coordinate system.

Figure 3 shows the Morlet wavelet-based power spectral density (Torrence & Compo, 1998) of the trace of magnetic fluctuations for the analyzed interval from the four Cluster spacecraft. The first and final four seconds of wavelet coefficients are removed to mitigate the effects of the cone of influence at small scales near the edges when calculating the power spectra. Some weak effect may be present at larger scales (for  $f < 10^{-2}$  Hz), which are only marginal to the scope of this work. Here, within the frequency range [0.01, 0.1] Hz, the spectrum has a spectral index of  $-1.50$ . At scales smaller than ion scales, within the frequency range [3, 20] Hz, the spectrum follows the  $-2.8$  power-law, typical for sub-ion scales between 0.3 and 1 AU (Alexandrova et al., 2008, 2009, 2012, 2021; Chen, Horbury, et al., 2010; Chen, Wicks, et al., 2010; Sahraoui et al., 2013). There is not a clear break at ion scales in this case (e.g., see the reviews of Alexandrova, Chen, et al. (2013), Sahraoui et al. (2020)). However, if power-laws are fitted for the inertial and sub-ion ranges, their intersection is found at 0.35 Hz. This frequency is close to the combined scale (denoted as  $f_{\rho_i + d_i}$ ) which is at 0.30 Hz (e.g., Bruno & Trenchi, 2014), defined as described below. The ion inertial scale is defined as  $d_i = V_A / \Omega_{ci}$ , where  $V_A = B / \sqrt{\mu_0 n_i m_i}$  is the Alfvén speed in units of km/s and  $\Omega_{ci} = qB/m_i$  is the cyclotron frequency in angular units of rad/s. The ion Larmor radius is defined as  $\rho_i = v_{thi\perp} / \Omega_{ci}$  (also in angular units of km/rad), where  $v_{thi\perp} = \sqrt{\frac{2k_B T_{i\perp}}{m_i}}$ . The combined scale is given as the sum of the ion Larmor and ion inertial lengths  $\rho_i + d_i$  (Bruno & Trenchi, 2014). This scale is associated with cyclotron resonance. If we consider a parallel propagating Alfvén wave with the dispersion relation  $\omega^2 = k_{\parallel}^2 V_A^2$ , and the cyclotron resonance condition is given by  $\omega - k v = \pm \Omega_{ci}$ , then the resonant wavenumber (in units of rad/km) will be  $k = \Omega_{ci} / (V_A + v_{th})$  when using the thermal speed as the velocity in the resonant condition. This can be written as  $k = (\rho_i + d_i)^{-1}$  (e.g., Bruno et al., 2014; Chen, Sorriso-Valvo, et al., 2014; Duan et al., 2020; Leamon et al., 1998). We remark here that it is important to be aware of units when comparing the characteristic scales to spacecraft separations, as often spatial scales are quoted in angular units but radians are omitted. For comparison with frequency spectra, these scales are usually expressed as “Taylor shifted” frequencies for the inertial lengths  $\left(f_{d_{i,e}} = \frac{v_{sw}}{2\pi d_{i,e}}\right)$ , Larmor radii  $\left(f_{\rho_{i,e}} = \frac{v_{sw}}{2\pi \rho_{i,e}}\right)$  and combined scale for ions  $\left(f_{\rho_i + d_i} = \frac{v_{sw}}{2\pi(d_i + \rho_i)}\right)$ , which are all in units of  $s^{-1}$ .

At electron scales, if another break or a transition from a power law to an exponential morphology is present, this tends to be associated with the electron Larmor radius (Alexandrova et al., 2009, 2012, 2021; Sahraoui et al., 2013; Schreiner & Saur, 2017), rather than the other characteristic scales (i.e., the shifted inertial scale). However, in



**Figure 1.** Measured data from Cluster 4 starting at 2015-02-15 21:25 (a) magnetic field from fluxgate magnetometer, (b) solar wind bulk speed from Cluster ion spectrometry's (CIS)/COmposition and DIstribution Function (CODIF) (black line) and Cluster ion spectrometry's (CIS)/hot ion analyzer (HIA) (red line) (c) electron density from plasma electron and current experiment (PEACE), (d) ion temperature from CIS/CODIF (black line) and CIS/HIA (red line), (e) electron temperature from PEACE, (f) ion plasma  $\beta$ , (g) electron plasma  $\beta$ . In panels (b, d, and f), ion measurements from CODIF (black) on C4 and HIA from C1 are displayed (red). The peak in the ion measurements is likely to be instrument-related rather than physical.

this particular case, the  $\text{SNR} = 3$  is at  $f_{\text{Max}} = 50$  Hz (the maximum physical frequency (Alexandrova et al., 2010)), which is close to  $f_{pe}$  and thus the spectral change at electron Larmor radius can not be measured. The STAFF-SC noise floor for the trace spectrum (gray dotted line) is determined using a burst mode interval on 2007-06-30 15:02–15:05, in the magnetospheric lobe, as was done by Kiyani et al. (2013). It is important to note that in the original interval used by Kiyani et al. (2013) there are some whistler waves at the start of the interval near 30 Hz, which give a slight bump between 2007-06-30 15:00–15:02 UT. We avoid this time in the interval to obtain lobe

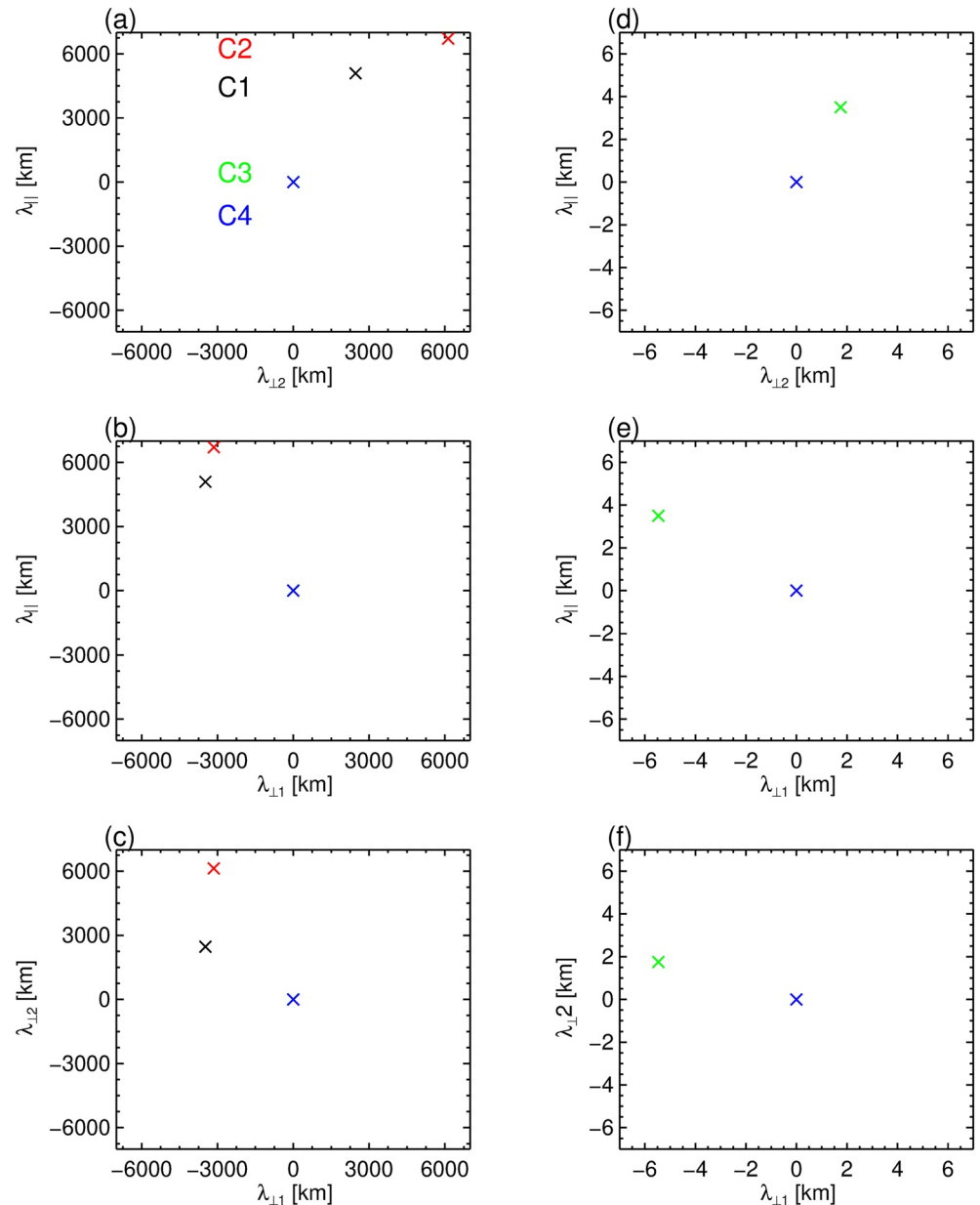


**Figure 2.** (a–c) Configuration of the four Cluster spacecraft relative to the location of C4 in mean field/bulk flow coordinates:  $e_{\parallel}$  is the unit vector along  $B_0$ ,  $e_{\perp 1} = \frac{e_{\parallel} \times V_{sw}}{|e_{\parallel} \times V_{sw}|}$ ,  $e_{\perp 2}$  completes the right hand coordinate system. The mean magnetic field direction is  $B_0 = [0.59, -4.15, 7.32]$  nT and the mean ion bulk velocity direction is  $V_{sw} = [-335, 35, 0]$  km/s in GSE co-ordinates. Figures (d–f) give a closer view of C3 and C4.

spectra which better approximates the noise. A dot-dashed gray line denotes three times the noise level. The intercept of this line with the measured spectrum gives  $f_{Max}$ . Above this frequency, the influence of noise is too large for the spectrum's results to be physically meaningful. The SNR is defined as  $SNR = Power/Power_{Lobe}$ , where  $Power$  refers to the trace power, individual components may have a lower SNR (see Appendix A).

An arrow in Figure 3 denotes the frequency  $v_{sw}/\lambda_{3d} = 50$  Hz, which, when converted to a spatial scale, corresponds to the inter-spacecraft distance of 7 km (i.e., the closest integer time lag that corresponds to a spatial lag of 7 km). This frequency is close to  $f_{Max}$  and  $f_{pe}$ . However, it should be noted that the spatial lag estimated from Taylor's hypothesis (along the flow direction) and the baseline (transverse to the flow), although equal in magnitude, have different orientations. It should be noted that in the high-frequency range Taylor's hypothesis could

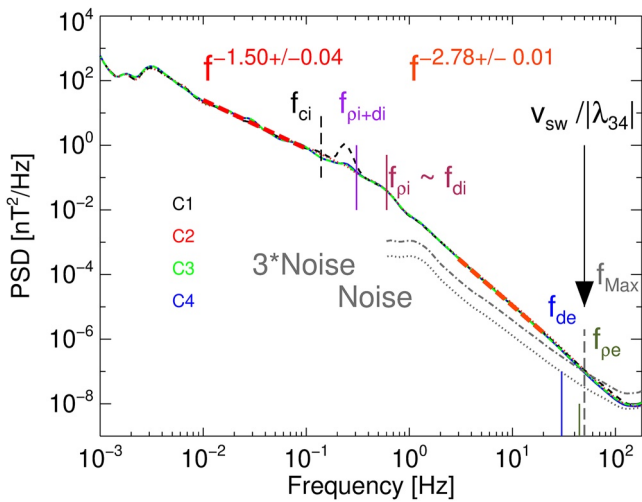


**Figure 3.** Total power spectral densities of magnetic fluctuations as a function of the satellite frame frequency as observed by Cluster spacecraft, calculated using merged fluxgate magnetometers and spatio temporal analysis of field fluctuations data. The different Cluster spacecraft are indicated by black dashed (C1), red dotted (C2), green dot dashed (C3) and solid blue (C4 lines) and all are similar except for C1 where there is some excess spin tone visible. The vertical lines denote the ion cyclotron frequency,  $f_{ci} = qB/2\pi m_i = 0.13$  Hz (black-dashed line) the shifted combined scale ( $f_{pi+di} = 0.3$  Hz purple), ion inertial ( $f_{di} = v_{sw}/2\pi d_i = 0.60$  Hz), and Larmor ( $f_{pe} = v_{sw}/2\pi \rho_i = 0.62$  Hz) (dark red and almost at the same frequency) radius scales. Merging frequencies are at the high-frequency end of the ion scales, [0.6, 1.5] Hz. The electron inertial ( $f_{de} = v_{sw}/2\pi d_e = 30$  Hz blue) and Larmor radius ( $f_{pe} = v_{sw}/2\pi \rho_e = 44$  Hz green) are also indicated. The dotted gray curve denotes the trace magnetic spectrum of a quiet interval of magnetic lobe plasma (2007-06-30 15:02-15:05 UT), which gives a good proxy for the instrumental noise. The dark gray dashed-dotted curve denotes three times the noise level. The vertical dashed gray line denotes 50 Hz, where SNR = 3 and the instrumental noise starts to influence the solar wind spectrum. Two power-law fits are performed at magnetohydrodynamic scales for  $f \in [0.01, 0.1]$  Hz and at sub ion scales for  $f \in [3, 20]$  Hz. The break frequency where they intersect is at 0.36 Hz close to the combined scale. The arrow denotes the timescale that corresponds to the inter-spacecraft distance  $v_{sw}/\lambda_{34}$  such that the distance along the stream direction and the baseline are equal. Note that this assumes Taylor's hypothesis.

break down if highly dispersive waves such as fast magnetosonic waves are present (Howes et al., 2014). We have no indications of either broadband magnetosonic waves which would cause a severe flattening of the magnetic field power spectrum (e.g., Klein et al., 2014) or narrow band whistlers (e.g., Lacombe et al., 2014; Roberts, Alexandrova, et al., 2017) which can cause a bump in the spectrum. In the limit of large wavenumbers kinetic Alfvén waves can become dispersive, however they are not expected to violate Taylor's hypothesis (Howes et al., 2014; Klein et al., 2014). Furthermore, the angle  $\theta_{BV}$  in the interval is close to  $90^\circ$  so that dispersive effects are expected to be well mitigated (Perri et al., 2017).

Let us consider the scale of 7 km, which is fixed by the satellites positions,  $\lambda = \lambda_{baseline}$ , and the time scale of  $\tau = 0.02$  s corresponding to the spatial scale along the flow  $|\lambda_{stream}| = |\lambda_{baseline}|$ , by assuming Taylor's hypothesis.

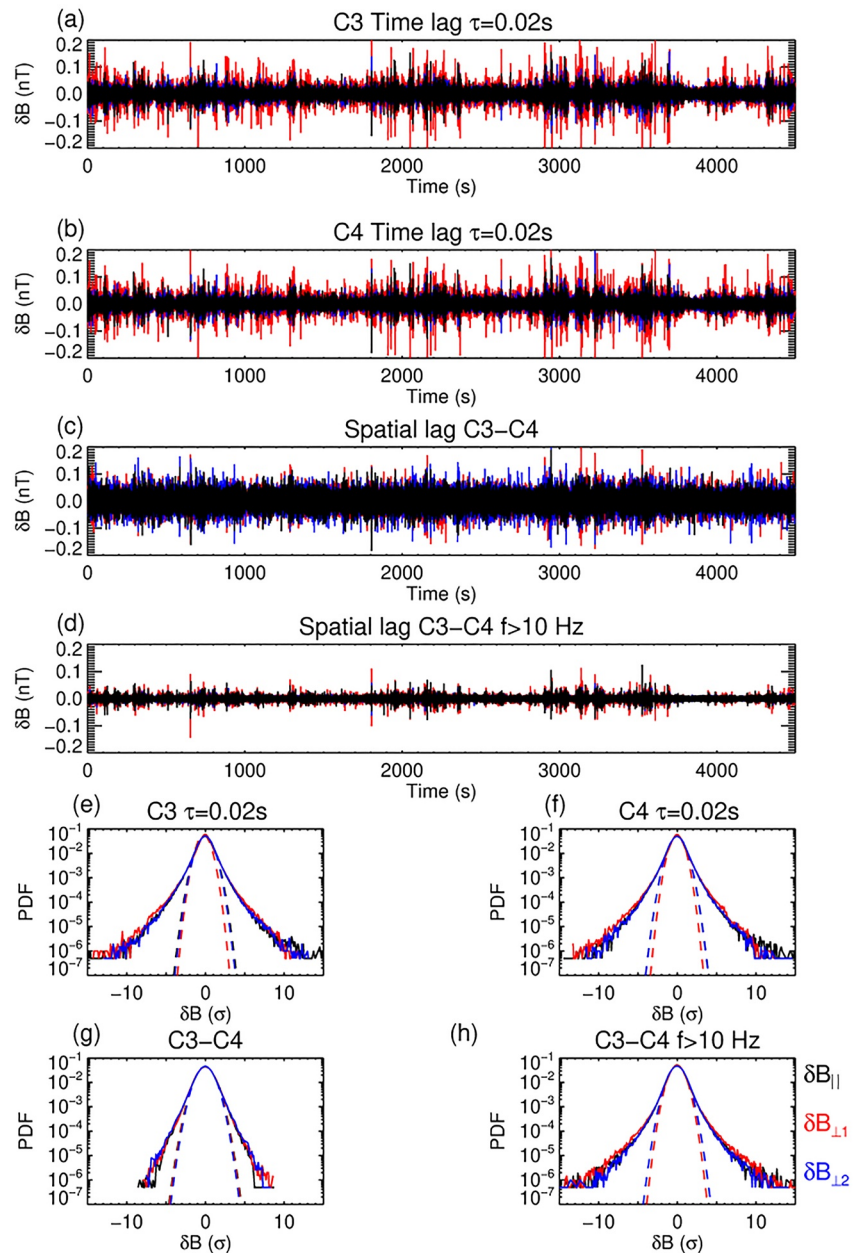
Figures 4a and 4b show the time series of the components of  $\delta B(\tau = 0.02$  s,  $t)$  for C3 and C4 in the local magnetic field–bulk velocity coordinate system, see Equations 5–8. The corresponding PDFs are shown in Figures 4e and 4f. It is clear that the time-lag-based increments from the two spacecraft are anisotropic and intermittent. The standard deviations for  $\delta B(\tau, t)$  are component dependent and similar on both satellites:  $[\sigma_{\parallel, C3}, \sigma_{\perp 1, C3}, \sigma_{\perp 2, C3}] = [0.010, 0.018, 0.011]$  nT and  $[\sigma_{\parallel, C4}, \sigma_{\perp 1, C4}, \sigma_{\perp 2, C4}] = [0.009, 0.018, 0.011]$  nT. The kurtosis for 3 components on 2 satellites are  $[K_{\parallel, C3}, K_{\perp 1, C3}, K_{\perp 2, C3}] = [8.51, 10.14, 8.18]$ , and  $[K_{\parallel, C4}, K_{\perp 1, C4}, K_{\perp 2, C4}] = [8.63, 10.39, 7.63]$ .

Figures 4c and 4g give spatial lags  $\delta B(\lambda = 7$  km,  $t)$  and the corresponding PDF's in the same coordinate system at the time lags. Surprisingly, these PDF's are close to Gaussian distribution, and fluctuations seems to be isotropic:  $[\sigma_{\parallel}, \sigma_{\perp 1}, \sigma_{\perp 2}] = [0.020, 0.022, 0.022]$  nT. The  $K$  values for three components are  $[K_{\parallel}, K_{\perp 1}, K_{\perp 2}] = [4.12, 4.45, 4.86]$ . We interpret this as being due to low frequency noise of the STAFF-SC instrument. Instrumental noise is uncorrelated for different  $t$  and  $\lambda$ , and by taking a difference between two measurements (either by a time lag or a spatial lag), the uncertainty of the measurement due to noise will be added in quadrature. The noise is also frequency dependent, and when taking time lags, much of the low-frequency noise (i.e., noise fluctuations below  $f < 1/\tau$ ) is filtered out. However, for spatial lags, the noise is integrated over all frequencies. Therefore, when using a spatial increment, low-frequency noise will affect the increment more than when a temporal lag is used, see Appendix B. To mitigate the noise

effect we high-pass filter the data at 10 Hz. The results are shown in Figures 4d and 4h. The spatial increments calculated using the high pass filtered data have standard deviations of  $[\sigma_{\parallel}, \sigma_{\perp 1}, \sigma_{\perp 2}] = [0.0046, 0.0053, 0.0041]$  nT, and kurtoses of  $[K_{\parallel}, K_{\perp 1}, K_{\perp 2}] = [8.75, 10.85, 7.18]$  which agree much better with the time lags. For the remainder of the paper spatial lags in the sub ion range will be high-pass filtered at 10 Hz. For larger scales this is not required as the fluctuations have significantly larger amplitudes.

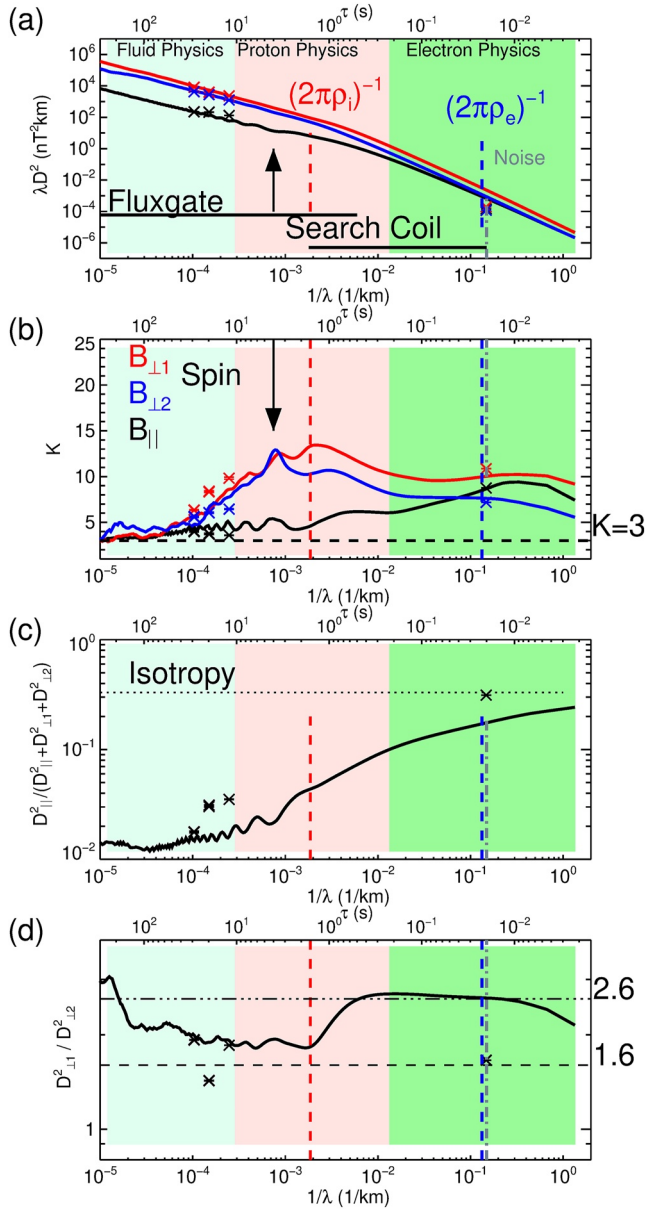
Figure 5a shows the second-order structure function  $D^2 = \langle |\delta B|^2 \rangle$  expressed as an equivalent spectrum  $\lambda D^2$ , as a function of inverse spatial scale  $1/\lambda$  in  $\text{km}^{-1}$ . Here  $\lambda$  refers to either the streamwise spatial scale  $\lambda_{stream}$  (based on Taylor's hypothesis to convert a single spacecraft time lag to a spatial lag,  $\lambda_{stream} = v_{sw}\tau$ ) or the inter-spacecraft distance  $\lambda_{baseline}$ . As for Figure 4, the local magnetic field–bulk velocity coordinate system is used, see Equations 5–8. The structure-functions of the time-lagged values, which are in the stream direction, are shown by solid lines, while the spatially-lagged structure functions, which have different orientations depending on which spacecraft pair is used, are denoted by crosses. The spatial lags cover both fluid and electron scales but are missing the ion scales. There is good agreement between space and time-lags structure functions. Note that there is also some spin effect observable in the parallel component at large scales.

Table 2 gives the spectral indices obtained from (a) second order structure functions in the local mean field frame, Figure 5, and (b) the wavelet spectra calculated in the global field frame. The observed differences are likely



**Figure 4.** Temporal lags  $\delta B(\tau, t)$  from C3 (a) and C4 (b) at a timescale  $\tau = 0.02$  s, which correspond to  $V_{sw}\tau = 7$  km in the stream direction, with  $V_{sw} = 335$  km/s. The angle between the flow (sampling) direction and magnetic field is  $\theta_{BV} = 95^\circ$ . (c) Spatial lags  $\delta B(\lambda, t)$  at  $\lambda = 7$  km, the inter-satellite separation vector  $\lambda$  is oblique to the flow (with an angle of about  $\theta_{Vz} \approx 70^\circ$ ) and to the field,  $\theta_{Bz} = 115^\circ$ . (d) Spatial lags where the magnetic field time series have been high pass filtered at 10 Hz. (e) Probability distribution functions (PDFs) based on the temporal lags from C3. (f) PDFs based on the temporal lags from C4 (g) PDFs of the raw spatial lags. (h) PDFs of the high pass filtered spatial lags. All increments are shown in the local magnetic field–bulk velocity coordinate system, see Equations 5–8. Starting time corresponds to 2015-02-15 21:25:00 UT. The PDFs have been fitted with a Gaussian (dashed lines) which clearly reveal the heavy tails in panels (e, f, h).

due to the different methods of calculating the mean-field and to a limitation of the two-point structure-function in measuring steep spectra (Abry et al., 1995; Chen, Horbury, et al., 2010; Chen, Wicks, et al., 2010; Landi et al., 2019; Monin et al., 1975; Teodorescu et al., 2021). To overcome this limitation, three or five point structure functions could be calculated (e.g., Cho et al., 2019; Landi et al., 2019; Teodorescu et al., 2021; Wang et al., 2020). As we only have two spacecraft to calculate spatial lags, we restrict the analysis to two-point structure functions to enable comparison between temporal and spatial lags.



**Figure 5.** (a) Second-order structure functions expressed as an equivalent spectrum. The crosses denote the calculation from inter-spacecraft lags, while the curves denote the calculation from time lags from C4. Different colors refer to different magnetic field components (see legend in panel b). (b) The corresponding scale-dependent kurtosis crosses. The black arrow denotes the spin frequency of Cluster at 0.25 Hz. The red vertical line denotes the ion Larmor radius (in km), and the blue vertical line denotes the electron Larmor radius. The gray vertical line gives  $f_{\text{Max}} = 50$  Hz as in Figure 3. (c) The ratio of the parallel second order structure function to the trace structure functions. A line at 1/3 denotes isotropy. (d) The ratio of the structure functions between the two perpendicular components: the one perpendicular to the flow  $D_{\perp 1}^2$  over the one along the flow  $D_{\perp 2}^2$  in the plane perpendicular to the local magnetic field. Horizontal lines indicate mean spectral indices in the inertial range, 1.6, dashed line, and 2.6 in the sub-ion range, dashed-dotted line. The shaded regions indicate approximate ranges for the relevance of fluid, proton and electron scales. Note that the second  $x$  axis denoting the corresponding time lags only applies to the time lagged fluctuations. Error bars are estimated from 100 bootstrap resamplings, and are smaller than the plotted symbols.

In order to mitigate possible finite sample size effects on the convergence of the moments calculation (Chapman et al., 2005; Dudok de Wit, 2004; Dudok De Wit et al., 2013; Kiyani et al., 2006; Tennekes & Wyngaard, 1972), we initially use the semi-analytical method of Dudok de Wit (2004) to determine the maximum moment order that can be reliably estimated. At a timescale of 0.02 s for the GI interval, convergence is validated up to the fourth-order moment, confirming that the kurtosis can be safely computed. Additionally, following the method proposed by Kiyani et al. (2006), we recursively remove the largest outliers until the kurtosis is observed to converge. The removal of less than 0.1% of the data provides the desired convergence. Furthermore, we exclude the first and final four seconds of the time series to avoid large fluctuations associated with the linear interpolation near the edges.

In Figure 5b, the scale-dependent kurtosis is shown. There is agreement between the time and the spatial lags at large and small scales. The time-lagged values show an evolution, from nearly Gaussian statistics at large scales increasing until the ion Larmor radius to a value of  $K$  about 10–15 for transverse components. At smaller scales,  $K$  slightly decreases and remains flat at a moderate value about 10 for  $\delta B_{\perp 1}$ . Meanwhile, the  $\perp 2$  component decreases to  $K \approx 5$  and the compressive component increases to  $K \approx 10$ . A local peak is present near the spin value of 4 s, as indicated by the arrow.

Figure 5c shows the ratio of the parallel second order structure function ( $D_{\parallel}^2$ ) component to the trace second order structure function ( $D_{\parallel}^2 + D_{\perp 1}^2 + D_{\perp 2}^2$ ), a measure of magnetic compressibility. The compressibility evolves toward isotropy (value of 0.3) in the sub-ion range, consistent with the predictions for a kinetic Alfvén wave (Kiyani et al., 2013; Lacombe et al., 2017), but is also consistent with magnetic structures in pressure balance at scales where the ion velocity fluctuation is much smaller than to the electron velocity, that is, where Hall term  $J \times B$  (where  $J$  is the current density) becomes dominant over the ideal MHD term  $-V \times B$  (Matteini et al., 2020).

Figure 5d shows the ratio  $D_{\perp 1}^2 / D_{\perp 2}^2 = \langle |\delta B_{\perp 1}|^2 \rangle / \langle |\delta B_{\perp 2}|^2 \rangle$ . The observed non-gyrotropy of the fluctuations in the spacecraft frame, with  $|\delta B_{\perp 1}| > |\delta B_{\perp 2}|$  is consistent with  $k_{\perp}$  gyrotropic fluctuations in the plasma frame, (e.g., Bieber et al., 1996; Lacombe et al., 2017; Matteini et al., 2020; Saur & Bieber, 1999). Indeed, when fluctuation have  $\delta B_{\perp 1} = \delta B_{\perp 2}$  and gyrotropic wavevectors with  $k_{\perp} \gg k_{\parallel}$  in the plasma frame, then in the satellite frame, the ratio  $D_{\perp 1}^2 / D_{\perp 2}^2$  appears to be equal to the spectral index (e.g., Saur & Bieber, 1999), which we clearly observe at the sub-ion range.

### 3.2. Statistical Study

Figure 6 shows the scale-dependent kurtosis  $K(1/\lambda)$  for all the intervals presented in Table 1. Several different shapes of  $K(1/\lambda)$  can be seen. In 11 intervals out of 20 we see an increase of  $K$  within the MHD range of scales and a plateau or a decrease at ion scales (intervals 1–4, 9–10, 13, 16–20). In 3 intervals out of 20 large kurtoses are seen in the compressible components at MHD scales (e.g., 5, 11, 14), most likely due to structures such as magnetic holes or mirror modes. Interval 7 shows quite low kurtosis throughout the scales of interest. These are likely quiet times with very few structures or where the SNR is low. In two other cases, the scaling of the kurtosis is more irregular (intervals 12 and 15). In this figure,  $K(1/\lambda)$  calculated using temporal lags are shown by continuous lines and based on the spatial lags are denoted by crosses, as in Figure 5b. In some cases, the two approaches

**Table 2**  
Spectral Indices  $\alpha$  for the Different Components of Magnetic Field Within the Inertial Range,  $f \in [0.1, 0.01]$  Hz ( $\tau \in [10, 100]$  s), and Within the Sub-Ion Range,  $f \in [3, 20]$  Hz ( $\tau \in [0.05, 0.33]$  s), for Two Different Approaches Used in This Work

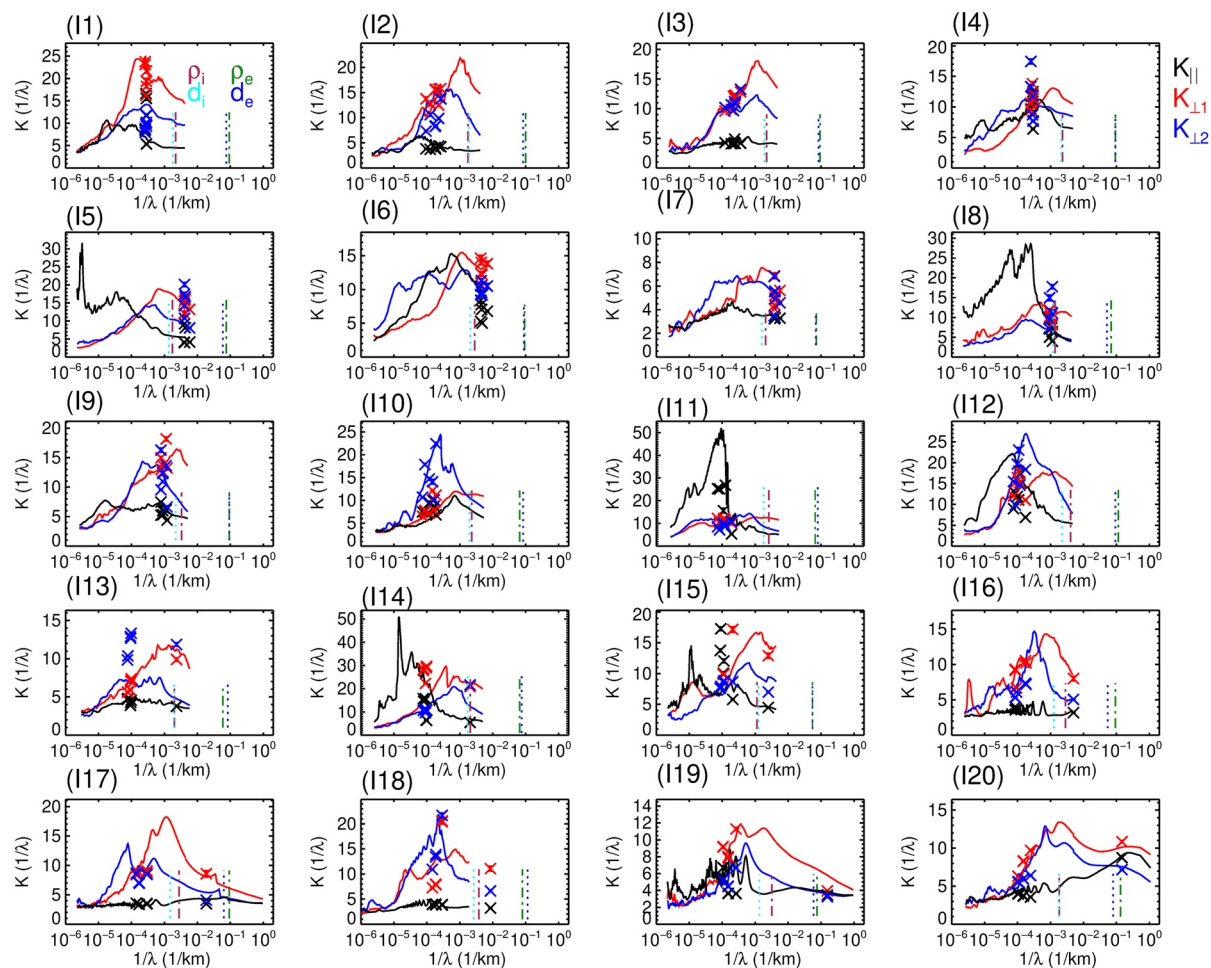
Structure functions (local field)	$\alpha_{\parallel}$	$\alpha_{\perp 1}$	$\alpha_{\perp 2}$
Inertial range	$-1.38 \pm 0.01$	$-1.61 \pm 0.01$	$-1.55 \pm 0.01$
Sub-ion range	$-2.32 \pm 0.01$	$-2.63 \pm 0.01$	$-2.62 \pm 0.01$
Wavelet spectra (global field)			
Inertial range	$-1.41 \pm 0.04$	$-1.49 \pm 0.03$	$-1.51 \pm 0.03$
Sub-ion range	$-2.64 \pm 0.01$	$-2.66 \pm 0.01$	$-2.70 \pm 0.01$

are in a good agreement (e.g., interval 2), while in others they do not (e.g., interval 1).

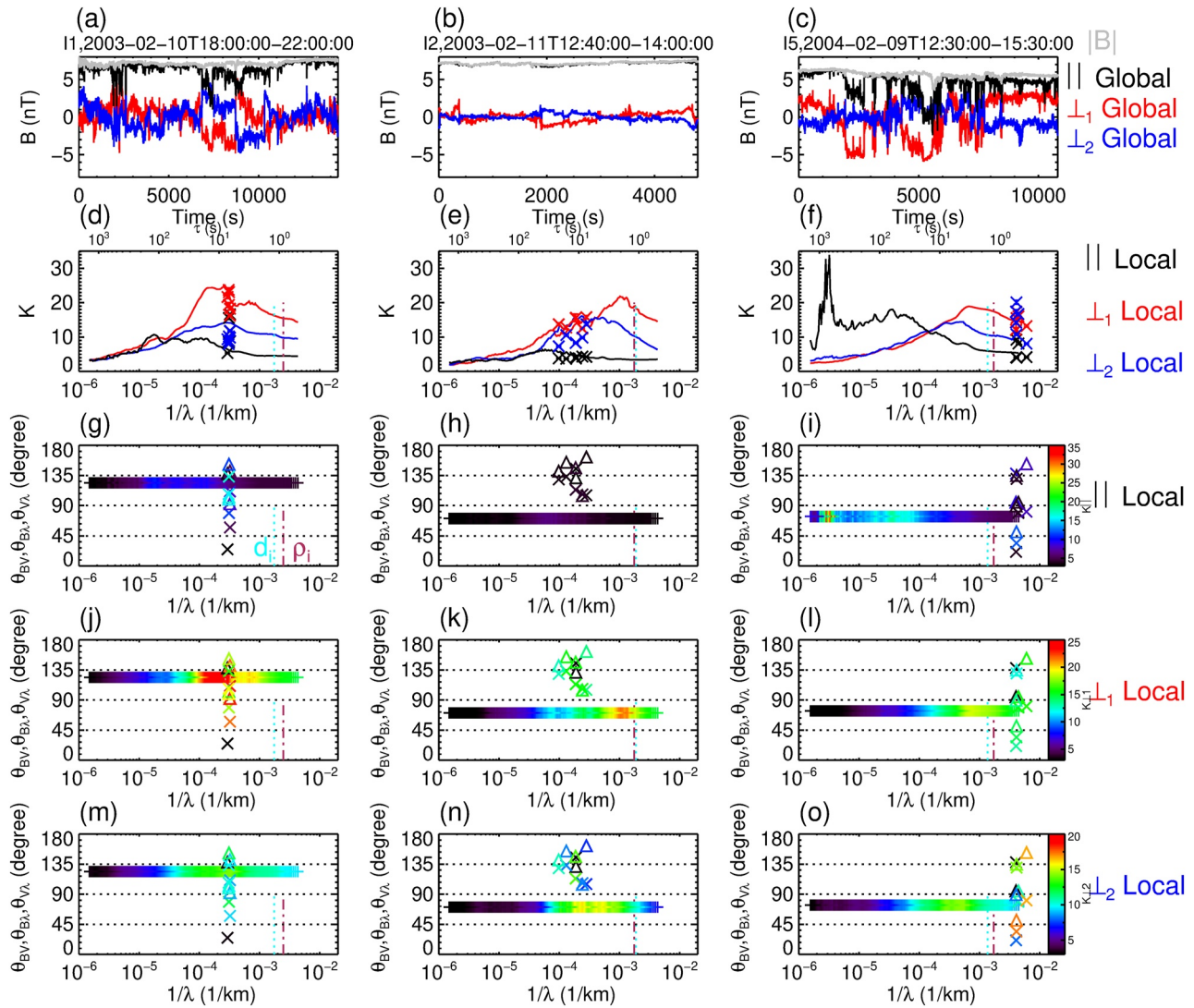
We investigate three cases (intervals 1, 2, and 5) further to understand the details of the relation between spatial and time lags. The corresponding time series of the magnetic field in global mean field coordinate systems are shown in Figures 7a–7c. We report here as well (panels (d, e, f)) the same information on  $K(1/\lambda)$  as in Figure 6. The three different intervals will now be compared in more detail.

Figure 7d shows the kurtosis for an interval with an increase at inertial range and a plateau or a decrease at ion scales. The spatial-lag-based kurtosis (from all 6 baselines) shows a broad range of values, but the measurements are limited in their scale coverage. The formation of the spacecraft in this case is a regular tetrahedron, so all baselines have similar magnitudes, but their orientations are different.

Figure 7e shows an example of similar behavior in the time-lag-based kurtosis; however, the spatial-lags cover a more extensive range of spatial scales. Here, the four Cluster spacecraft are in a more elongated “knife-edge” or “linear” formation, meaning that better agreement is found with the time lags as the baselines are approximately



**Figure 6.** Scale dependent kurtosis  $K(1/\lambda)$  for 20 intervals of Table 1. Lines denote  $K(1/\lambda)$  calculated from time lags and expressed as their streamwise spatial scale and the points denote the calculation based on spatial lags. Black denotes,  $K_{\parallel}$ , red denotes,  $K_{\perp 1}$  and blue denotes  $K_{\perp 2}$ . The vertical lines denote the proton and electron characteristic scales.



**Figure 7.** (a–c) Magnetic field time series in the global mean field aligned coordinates for three intervals (I1, I2, and I5) of Tables 1d–1f. The corresponding scale dependent kurtoses in the local coordinate systems (the same information as in Figure 6(I1, I2, and I5)). (g–o)  $K(1/\lambda, \theta)$ , with  $\theta$  being the angle between the sampling direction and the mean magnetic field  $\theta_{BV}$  (lines), between the magnetic field and the spacecraft baseline  $\theta_{B\lambda}$  (crosses), or the angle between the spacecraft baseline and the bulk flow  $\theta_{V\lambda}$  (triangles). The color bars give the kurtosis. Here  $\lambda$  refers to  $\lambda_{stream}$  for the lines and  $\lambda_{baseline}$  for the crosses.

oriented along the velocity direction, that is,  $\theta_{BV} \sim \theta_{B\lambda}$ . The range of accessible spatial scales is improved with this formation at the cost of directional coverage. This is an inherent limitation of having only four sampling points.

A third example is shown in Figure 7f, where there is an extremely strong compressive component kurtosis at large scales. When the time series are inspected visually in Figure 7c, we see a significant depression in the magnetic field magnitude near the center of the interval. This could be classified as a magnetic hole and is likely the cause of the large kurtosis of  $\delta B_{\parallel}$ .

To investigate the anisotropy of the kurtosis we present it in an alternative way in Figures 7g–7o. Here the  $x$ -axis denotes the scale, and the  $y$ -axis denotes the angle. In the case of the time lag the angle is  $\theta_{BV}$ , for spatial lags the angles shown are  $\theta_{B\lambda}$  (crosses) and  $\theta_{V\lambda}$  (triangles). The colors of the symbols denote the kurtosis. Displaying the data in this way allows the variation due to scale and due to anisotropy to be displayed. For the first case (panels (g, j, m) for three magnetic field components), there is good angular coverage from the regular tetrahedron. When the angles of the inter-spacecraft baseline and the magnetic field ( $\theta_{B\lambda}$ ) are far from  $90^\circ$  the corresponding kurtosis tends to be smaller. In the first case the smallest value of kurtosis from a spatial lag occurs when  $\theta_{B\lambda} \sim 20^\circ$  and the largest when  $\theta_{B\lambda} \sim 90^\circ$  (e.g., panels g, j, m). In column 2, panels (h, k, n),

we see more spatial coverage which matches the time lags better than the first cases and the angular range is more limited. This suggests that the differences are due to the wavevector anisotropy of the fluctuations. In column 3, panels (i, l, o), the comparison is possible only at sub-ion scales:  $K(\delta B_{\parallel})$  and  $K(\delta B_{\perp 1})$  are similar for space and time lags, no effect of possible  $k$ -anisotropy is observed;  $K(\delta B_{\perp 2})$  of spatial lags is a bit higher than for time lags all over the angular coverage.

#### 4. Summary and Discussion

In this work, we have done a study of 20 slow solar wind streams at 1 AU with four satellites of Cluster mission to investigate scale-dependent kurtosis  $K(1/\lambda)$  from MHD up to electron scales. We have used FGM measurements at MHD scales and STAFF-SC at kinetic scales. The data set covers different satellites separations and configurations. We have compared  $K$  of magnetic field time and spatial increments. We observe a good agreement between the time and spatial lags even at sub-ion scales. This is different with the results of Chasapis, Matthaeus, Parashar, Fuselier, et al. (2017), Chasapis, Matthaeus, Parashar, LeContel, et al. (2017), where in the sub-ion range the kurtosis of spatial lags was found to be significantly larger than the time lags.

We see two explanations of this controversy: (a) to resolve  $K$ , which is the fourth order moment,  $10^5$  data points are needed, see the rule of thumb in Dudok De Wit et al. (2013), Equation 8, that is not verified in the study of Chasapis, Matthaeus, Parashar, Fuselier, et al. (2017), Chasapis, Matthaeus, Parashar, LeContel, et al. (2017) and likely the results may represent more local phenomena (due to the shorter intervals) that are not sampled sufficiently in the time series; (b) the STAFF-SC of Cluster is more sensitive than the MMS fluxgate magnetometer to resolve kinetic scales in the solar wind.

Using the classical definition of spatial lags, Equation 3 applied on the raw data on two satellites, at kinetic scales, we have found important differences with time-lag fluctuations: PDF of  $\delta B(t, \tau)$  are strongly non-Gaussian, but PDF's of  $\delta B(t, \lambda)$  are quasi-Gaussian, as was already observed by Chhiber et al. (2018), Roberts, Thwaites, et al. (2020).

This apparent difference between space and time lags at small scales comes from the dominance of the instrumental noise. Indeed, calculating time lags using the same satellite, the influence of low frequency noise is subtracted. While, calculating space lags using 2 satellites, the uncorrelated noise is added. See Appendix B for more details. The noise of STAFF-SC is frequency dependent and important at lowest frequencies. To avoid this low-frequency noise we apply the high pass filter at 10 Hz on STAFF-SC data. Then, we calculate  $\delta B(t, \lambda)$  which appears to have similar statistics as  $\delta B(t, \tau)$ . For example, for the GI time interval studied in details in the paper,  $K$  values are the same for time and space lags at electron scales. More generally, at different scales, we find a good agreement (for 13 out of 20 intervals). The observed differences for other seven intervals can be explained by wavevector anisotropy of turbulent fluctuations.

Regarding scale-dependent behavior of  $K$ , we observe an increase at MHD scales and then reduces or plateaus in the sub-ion range, see Figures 5 and 7, consistent with the results of Kiyani et al. (2009), Chen, Sorriso-Valvo, et al. (2014), Chen, Leung, et al. (2014), Chasapis, Matthaeus, Parashar, Fuselier, et al. (2017), Chasapis, Matthaeus, Parashar, LeContel, et al. (2017), Chhiber et al. (2018), Carbone et al. (2018), Chhiber et al. (2021). This is different from what is typically observed in planetary magnetosheaths (Alberti et al., 2021; Bowen et al., 2021; Chhiber et al., 2018; Tao et al., 2015; von Papen et al., 2014; Yordanova et al., 2020). However, there are some observations of weak intermittency in planetary magnetosheaths behind the quasi-perpendicular shock (e.g., Hadid et al., 2015), where ion instabilities may be at work to reduce strong temperature anisotropy. Another example of weak intermittency was observed during intervals with Kelvin-Helmholtz waves (Quijia et al., 2021), where again the presence of waves may mix-up phases and thus reduce kurtosis of the fluctuations.

Understanding the differences in the two plasma environments, solar wind and the magnetosheath, may shed light on the physical mechanisms that cause the different kurtosis signatures. Magnetosheath plasma is characterized by much stronger fluctuation amplitudes, larger temperatures, temperature anisotropies and plasma  $\beta$  due to processing at the shock. This raises two possibilities: (a) the instrumental noise affects the measurements in the solar wind or (b) there is a physical mechanism that causes the reduced intermittency (or conversely the absence of a physical mechanism in the solar wind).

In Figure 3 we have seen that the spectrum is above three times the noise floor up to the shifted spatial scale corresponding to the inter-spacecraft distance  $v_{sw}/\lambda_{34}$ , which is close to the Doppler shifted  $\rho_e$ . Therefore we do not expect the flattening at ion scales to be due to instrumental noise.

There must be physical mechanisms in the solar wind which are responsible for the reduced kurtosis at kinetic scales. As in the quasi-perpendicular magnetosheath, waves at ion scales could destroy the cross scale coupling (e.g., Alexandrova, 2005; Bruno et al., 2003; Carbone et al., 2021). An alternative may be that MHD-scale structures cannot persist into the sub-ion range (Lion et al., 2016), that is, structures are destroyed or smoothed-out by dissipation (Mallet et al., 2019) at a certain scale. An example would be a current sheet reconnecting as it thins and becomes unstable to the tearing instability (e.g., Mallet et al., 2011), which would see a current sheet at the disruption scale destroyed, “resetting” the intermittency before structures may be generated again by an electron-scale cascade. See also the discussion of Cerri et al. (2019). However, reconnection may also inject energy and structures back into the turbulence (e.g., Franci et al., 2017). It is also possible that there may be structures in planetary magnetosheaths that can exist at electron scales, such as electron scale current sheets (Yordanova et al., 2016), vortices Jovanović et al. (2015), and electron-only reconnection (Phan et al., 2018), electron holes (Haynes et al., 2015), whereas they may be less frequent or less energetic in the solar wind (Alexandrova et al., 2020; Perri, Goldstein, et al., 2012). For example, a local study of the GI time interval analyzed here, was done in Alexandrova et al. (2020). The authors showed the presence of an electron scale vortices observed at both C3 and C4, which seems to make up the majority of intermittent electron scale structures.

When we look at  $K(1/\lambda)$  of different intervals in Figure 6, sometimes we see a strong increase in kurtosis for the compressive component (black curves), similar to what has been observed in Bruno et al. (2003). This can be due to large-scale compressive structures at fluid scales such as magnetic holes in the example shown in Figures 7c and 7f.

At ion scales, the transverse components become more intermittent, which reflects that coherent structures in this range are predominantly incompressible, such as current sheets or Alfvén vortices (e.g., Lion et al., 2016; Perrone et al., 2017; Roberts et al., 2016). There is also a difference in the two transverse components, with the flow direction component having a lower kurtosis and the mean peak of kurtosis occurring at larger scales.

In Figure 6, we have compared the 20 intervals with various baseline directions and sizes. Significant variability is observed between intervals in terms of time lagged kurtoses, and in terms of the relation of spatial lags to the time lags. When spacecraft are aligned with the flow, we see good agreement between the time and spatial lags, like in interval 2, Figures 7e, 7h, 7k, and 7n). This is expected as there will be a smaller angle between  $\lambda_{stream}$  and  $\lambda_{baseline}$  when the spacecraft are in a more linear formation. For more regular tetrahedral configurations where baselines can be transverse to the flow, there is more variation in the kurtosis values due to the wavevector anisotropy, like in interval 1, see Figures 7d, 7g, 7j, and 7m.

Even though we have controlled for some plasma parameters, there may be some intervals that contain more or fewer structures, which emphasize the need for multi-spacecraft, multi-scale measurements (Dai et al., 2020; Klein et al., 2019; Matthaeus et al., 2019; Montgomery, 1980; Schwartz et al., 2011; Verscharen et al., 2021) of the same interval. Future mission design should prioritize having many different baselines with different sizes and directions, such as the Helioswarm concept (Klein et al., 2019) or the self-adaptive magnetic reconnection explorer (e.g., Dai et al., 2020). Furthermore, a search-coil magnetometer with a higher SNR would be desirable for studying electron-scale solar-wind turbulence (e.g., Vaivads et al., 2016).

To summarize, the GI 2015–2016 Cluster campaign's magnetic field data have provided exceptional data for the study of sub-ion scale turbulence. During the campaign, the mission was in a configuration with two spacecraft at a distance of the order of the electron gyroradius, while the other inter-spacecraft distances were of the order of MHD (fluid) scales. To obtain the necessary data to investigate anisotropic, multi-scale phenomena such as plasma turbulence we emphasize the need to go beyond tetrahedral formations of spacecraft in the future. The natural wavevector anisotropy require baselines at different angles to the field and flow, and the various characteristic time and length scales set a requirement for multi-scale coverage. A tetrahedral mission, such as Cluster, can accomplish this kind of study with many years of data; however, it is also limited as the only way to perform

this is to compare different plasmas. Future studies with Cluster at small scales should focus on having sufficient SNR, and should consider different orientations of the magnetic field with respect to the bulk flow and the spacecraft baselines.

### Appendix A: Influence of Instrumental Noise on Measurements at Kinetic Scales

The differences in the magnetosheath and the solar wind results at kinetic scales reported by Chhiber et al. (2018) are very likely due to instrumental noise. In that work, being in the magnetosheath, the signal-to-noise ratio (SNR) is much larger than in the solar wind. In the solar wind interval of Chhiber et al. (2018) the kurtosis revealed Gaussian fluctuations for  $f > 2$  Hz in the FGM instrument. It is typical for a FGM to be dominated by noise at these frequencies in the solar wind. In the study of Saturn's magnetosheath by von Papen et al. (2014) a flattening in the kurtosis is also seen for  $f > 0.5$  Hz and is due to the low SNR. If the intermittent fluctuations present in the solar wind are not sufficiently energetic to be above the instrumental noise, then the fluctuations will appear Gaussian.

Here we discuss Cluster/STAFF-SC noise and its potential effects on the results at kinetic scales. Figure A1 shows the power spectral densities (PSD) and the SNRs for the three GSE components of magnetic field measured by STAFF-SC between 1 and 200 Hz by comparing the wavelet spectra of the GI interval with the interval of lobe plasma discussed previously. Here the SNR for a  $i$ -component at each satellite (C3 and C4) is defined as the power of the  $i$ 'th GSE component over the power of the magnetic lobe interval for the same component  $SNR_i = PSD_i / PSD_{i, \text{Lobe}}$ . The arrow denotes the maximum physical frequency,  $f_{\text{Max}}$  used in this study, that is, for

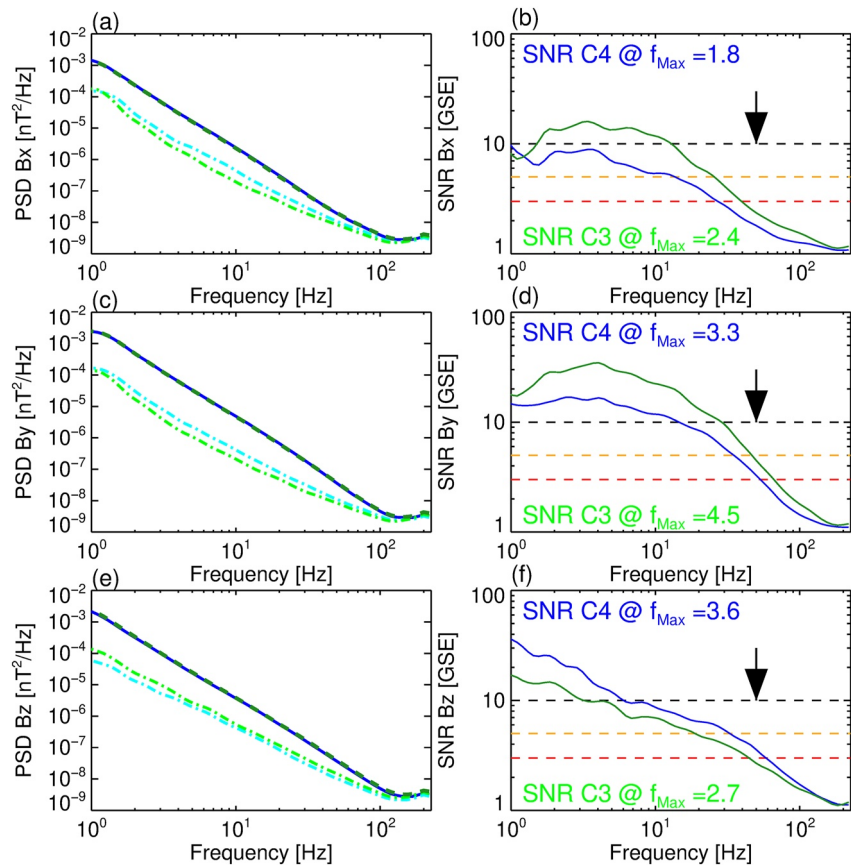


**Figure A1.** The Power spectral densities of the three GSE components of the magnetic field measured on C3 (dark green/dashed) and C4 (solid blue) (a–c) from interval 20 (note that the PDS's on C3 and C4 are nearly identical). The light green and cyan dot-dashed lines denote the estimated noise floor from the magnetic lobes for C3 and C4, respectively. Panels (d–f) show the corresponding signal-to-noise ratios. The horizontal lines denote signal to noise ratios of 10, 5, and 3, respectively.

**Table A1**

Cluster/Spatio Temporal Analysis of Field Fluctuations Sensitivity Levels at Various Frequencies in nT, Calculated With Equation A1, Using the Data of Kiyani et al. (2013) From the Magnetospheric Lobes

	1 Hz	30 Hz	50 Hz	77 Hz
$\sigma_{x,C3}$ (nT)	0.00557	0.00032	0.00027	0.00023
$\sigma_{y,C3}$ (nT)	0.00494	0.00032	0.00027	0.00023
$\sigma_{z,C3}$ (nT)	0.00486	0.00049	0.00035	0.00028
$\sigma_{x,C4}$ [nT]	0.00513	0.00040	0.00031	0.00026
$\sigma_{y,C4}$ (nT)	0.00540	0.00042	0.00031	0.00026
$\sigma_{z,C4}$ (nT)	0.00320	0.00040	0.00030	0.00025

Note. These values Are equivalent to standard deviations of magnetic field fluctuations in the lobes at different time scales.

$f < f_{\text{Max}}$  the trace power has SNR > 3, see Figure 3. The value of the SNR at this frequency for different components is also quoted on the plot.

For C3 and C4, PSD( $B_y$ ) has SNR > 3 at  $f_{\text{Max}}$  and SNR > 10 at  $f < 10$  Hz. So, the corresponding fluctuations are not much affected by the noise and thus the behaviour of  $K(1/\lambda)$  around ion scales and the plateau at sub-ion scales are likely physical rather than due to noise.

At electron scales, where SNR is close to 3, it is not so evident and more work should be done to study the influence of noise on high order statistics. The  $x$  component has a smaller SNR, this explains the difference in kurtosis in Figure 5b, where the  $B_{\perp 2}$  component has a smaller kurtosis than two other components. Future work will consider the SNR requisite for resolving intermittency.

We also consider the sensitivity of STAFF-SC at a fixed frequency  $f = 1/\tau$ . This can be used as an estimate of the error at a fixed frequency. If PSD<sub>noise</sub>( $f$ ) is the spectrum of STAFF-SC sensitivity, then we can write:

$$\sigma(f_{\text{fixed}}) = \sqrt{PSD_{\text{noise}}(f_{\text{fixed}}) * \Delta f}, \quad (\text{A1})$$

where  $\Delta f$  is the frequency resolution around  $f_{\text{fixed}}$  (e.g., Jagarlamudi et al., 2020). Table A1 gives error estimates at 4 frequencies for C3 and C4 and for three field components. The values are much smaller than the standard deviations of magnetic field fluctuations in the solar wind for the GI time interval, quoted in the text accompanying Figure 4. Thus, we can be confident that magnetic field measurements during this GI interval are not affected by instrumental noise at  $f < 50$  Hz.

## Appendix B: Influence of Instrumental Noise on Spatial Lags

Let us consider the magnetic field  $B_1(t, \lambda_1)$  and  $B_2(t, \lambda_2)$  measured at two points in space to be a superposition of a “true” magnetic field  $B_{1,\text{true}}, B_{2,\text{true}}$  and a noise  $\sigma_1, \sigma_2$ . If these noises are independent (as would be expected for measurements on different spacecraft), for a spatial increment  $\delta B(t, \lambda_{12}) = B_1(t) - B_2(t)$  the error will be:

$$\sigma_{12} = \sqrt{\sigma_1^2 + \sigma_2^2} \quad (\text{B1})$$

If the noise at two points in space is of the same order (or from the same instrument in the case of a time lag) then  $\sigma_1 \approx \sigma_2 \approx \sigma$ , such that  $\sigma_{12} = \sqrt{2}\sigma$ .

However, when time lags are taken much of the low frequency noise  $P_{\text{noise}}(f < 1/\tau)$  (that dominates in terms of amplitude) is removed. When considering spatial lags the noise is integrated over all frequencies. Thus time increments are much less affected by the instrumental noise than space increments, which explains the differences in Figure 4 between the PDF's of the time lags and of the raw spatial lags.

Table B1 gives standard deviations of the magnetic field fluctuations  $B(t)$  measured by STAFF instruments on C3 and C4 in the lobes of the Earth's magnetosphere (used as a proxy of the in-flight noise) and the errors on the space increments calculated using Equation B1. These values are close to the standard deviations of magnetic fluctuations in the solar wind given in the discussion of Figure 4. Thus, the raw spatial increments at kinetic

**Table B1**

(Left Column) The Standard Deviations of the Magnetic Field Measurements  $B(t)$  of Cluster/Spatio Temporal Analysis of Field Fluctuations (STAFF-SC) in the Magnetic Lobes of Earth on C3 and C4, Which Corresponds to the Integrals Over All Frequencies of the STAFF-SC Sensitivity

	All frequencies	$f > 10$ Hz
$\sigma_{B_x,C3}$ (nT)	0.013	0.0014
$\sigma_{B_y,C3}$ (nT)	0.012	0.0014
$\sigma_{B_z,C3}$ (nT)	0.012	0.0020
$\sigma_{B_x,C4}$ (nT)	0.015	0.0018
$\sigma_{B_y,C4}$ (nT)	0.015	0.0018
$\sigma_{B_z,C4}$ (nT)	0.008	0.0018
$\sigma_{B_x,C3C4}$ (nT)	0.019	0.0022
$\sigma_{B_y,C3C4}$ (nT)	0.019	0.0022
$\sigma_{B_z,C3C4}$ (nT)	0.015	0.0026

Note. (Right column) the values of the standard deviations for STAFF-SC in the lobe when the signals are high pass filtered at 10 Hz.

scales are strongly affected by the noise, especially, their thermal part around zero. High amplitude spikes visible in spatial lags in Figure 4c are of similar amplitudes as the spikes in temporal lags, so the energetic events can be captured by spatial lags as well. However, as far as the noise here is much higher than for time lags, the results of the kurtosis calculations are questionable.

The standard deviations shown in Table B1 contain fluctuations from all STAFF-SC frequencies. As such they will be dominated by low frequency fluctuations, see Figures A1a, A1c, and A1e. We now discuss how to reduce the effects of low frequency noise.

If we consider two magnetic field measurements at two satellites,  $B_1$  and  $B_2$ , which are a superposition of low frequency signal  $B_{L,S,1,2}$  and noise  $\sigma_{L,1,2}$ , and high frequency signal  $B_{H,S,1,2}$  and noise  $\sigma_{H,1,2}$  then:

$$\begin{aligned} B_1 &= B_{L,S,1} + \sigma_{L,1} + B_{H,S,1} + \sigma_{H,1} \\ B_2 &= B_{L,S,2} + \sigma_{L,2} + B_{H,S,2} + \sigma_{H,2} \end{aligned} \quad (\text{B2})$$

Taking a spatial lag without high pass filtering will result in

$$\begin{aligned} B_1 - B_2 &= (B_{L,S,1} - B_{L,S,2}) + \sqrt{(\sigma_{L,1}^2 + \sigma_{L,2}^2)} + (B_{H,S,1} - B_{H,S,2}) + \sqrt{(\sigma_{H,1}^2 + \sigma_{H,2}^2)}, \\ &= \Delta_{L,S} + \sqrt{2}\sigma_L + \Delta_{H,S} + \sqrt{2}\sigma_H \end{aligned} \quad (\text{B3})$$

where  $\Delta$  refers to the difference between two spacecraft for low  $L$  and high  $H$  frequency components of signal  $S$ . However, the noise components will add in quadrature as in Equation B1. Here we assume that the noise at two different points in space is of the same order and at a given satellite. The low frequency noise is denoted by  $\sigma_L$  and high frequency noise is denoted by  $\sigma_H$ . Note that we refer to low frequency as scales above the spacecraft separation, and high as scales smaller than the spacecraft separation. If we assume that the spatial lag will filter the low frequency signal then  $\Delta_{L,S} \approx 0$  and a spatial lag will be:

$$B_1 - B_2 = \Delta_{H,S} + \sqrt{2}(\sigma_L + \sigma_H) \quad (\text{B4})$$

The spatial lag will be dominated by noise if  $\sqrt{2}(\sigma_L + \sigma_H) > \Delta_{H,S}$ . However, the low frequency noise will have a much larger amplitude compared to the high frequency noise  $\sigma_L \gg \sigma_H$ . To mitigate the effect of the low frequency noise it is prudent to high pass filter the data,  $B_1$  and  $B_2$ , so that  $\sigma_L \approx 0$ . Note that filtering in this way may impact the spatial lag as some of the wanted signal may be filtered also. Therefore the cutoff frequency  $f_{\text{cutoff}}$  of the high

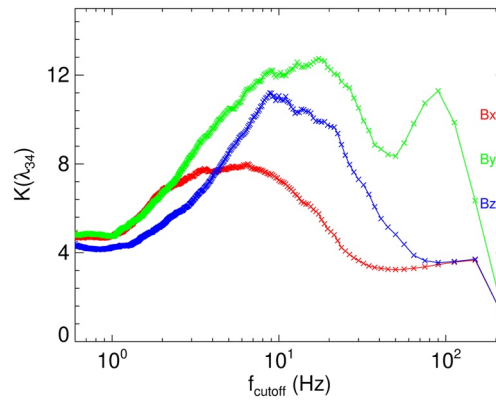


**Figure B1.** The kurtosis of spatial lags as a function of the high pass filter cutoff frequency.

pass filtering must be carefully selected for the spatial lag in question:  $f_{\text{cutoff}}$  should be high enough to filter noise, but low enough such that it is far away from the scale of spacecraft separation. Note that should the signal-to-noise ratio be larger ( $\Delta_{H,S} \gg \sqrt{2}(\sigma_L + \sigma_H)$ ) as is typical in the inertial range this process would not need to be applied.

The choice of which frequency to high pass filter is not straightforward. Taylor's hypothesis provides a method to convert a time-lag to a spatial lag. However, we cannot map a spatial lag to a time lag except when the two spacecraft are oriented along the flow direction. If we consider Equation B4, the noise terms  $\sigma_L$  and  $\sigma_H$  will act to reduce the kurtosis. Therefore, high pass filtering will begin by reducing  $\sigma_L$  thus increasing the kurtosis, before it begins to also filter  $\Delta_{H,S}$  (the signal we are interested in). When it begins to filter  $\Delta_{H,S}$  then the kurtosis will reduce. Therefore a prudent choice is to select a cutoff that maximizes the kurtosis.

Figure B1 shows the kurtosis of the spatial lags as a function of the high pass filter cutoff. We chose to filter the data at  $f_{\text{cutoff}} = 10$  Hz. This value was selected to ensure that the magnetic field components had close to maximum kurtosis, and is a compromise between the different components which peak at slightly different values of cut-off frequency. The corresponding errors  $\sigma_H$  are much smaller than the integrated noise over all frequencies, see Table B1.

Note that for the case of 7 km in Figure 4 the  $v_{\text{sw}}/\lambda_{3,4} = 50$  Hz, so the choice of 10 Hz is far from the corresponding frequency estimated from Taylor's hypothesis, so any effects from filtering the low frequency signal are expected to be minimal.

We are not aware that this issue has previously been discussed, and as such some results using two spacecraft lags (e.g., Chasapis, Matthaeus, Parashar, Fuselier, et al., 2017; Chasapis, Matthaeus, Parashar, LeContel, et al., 2017; Chhiber et al., 2018; Roberts, Thwaites, et al., 2020; Roberts, Verscharen, et al., 2020) should be reconsidered in the light of this limitation. Finally, we note that the discussions here are relevant for mission concepts such as Debye (Verscharen et al., 2021) and Helioswarm (Klein et al., 2019) that are proposed to have inter-spacecraft distances at or smaller than ion scales.

## Data Availability Statement

All the data from the Cluster spacecraft are available from the Cluster Science archive <https://csa.esac.esa.int/csa-web/>. The authors acknowledge the instrument teams of the FGM, STAFF, CIS and PEACE for providing excellent data over the last 20 years. The authors also acknowledge the Cluster Science Archive team for facilitating access to the data and all persons involved in mission operations. The OMNI data were obtained from the GSFC/SPDF OMNIWeb interface at <https://omniweb.gsfc.nasa.gov>.

## References

- Abry, P., Gonçalvès, P., & Flandrin, P. (1995). *Wavelets, spectrum analysis and 1/f processes*. In (pp. 15–29). [https://doi.org/10.1007/978-1-4612-2544-7\\_2](https://doi.org/10.1007/978-1-4612-2544-7_2)
- Alberti, T., Milillo, A., Laurenza, M., Massetti, S., Ivanovski, S. L., Ippolito, A., et al. (2021). Multiscale features of the near-Hermean environment as derived through the Hilbert-Huang transform. *Frontiers in Physics*, 9, 668098. <https://doi.org/10.3389/fphy.2021.668098>

## Acknowledgments

O.W.R. is grateful to Riddhi Bandyopadhyay for several comments that improved the manuscript. O.A. and P.C. thank CNES support for STAFF data processing and analysis. Z.V. was supported by the Austrian FWF under contract P28764-N27. R.N. was supported by Austrian FWF Project No. I2016-N20. L.S.-V. was funded by SNSA grants 86/20 and 145/18.

- Alexandrova, A., Nakamura, R., Panov, E. V., Sasunov, Y. L., Nakamura, T., Vörös, Z., et al. (2016). Two interacting X lines in magnetotail: Evolution of collision between the counterstreaming jets. *Geophysical Research Letters*, *43*(15), 7795–7803. <https://doi.org/10.1002/2016GL069823>
- Alexandrova, O. (2005). Turbulence MHD dans la magnétogaine terrestre en aval des chocs quasi-perpendiculaires.
- Alexandrova, O. (2008). Solar wind vs magnetosheath turbulence and Alfvén vortices. *Nonlinear Processes in Geophysics*, *15*(1), 95–108. <https://doi.org/10.5194/npg-15-95-2008>
- Alexandrova, O., Bale, S., & Lacombe, C. (2013). Comment on “evidence of a cascade and dissipation of solar-wind turbulence at the electron gyroscale”. *Physical Review Letters*, *111*(14), 149001. <https://doi.org/10.1103/PhysRevLett.111.149001>
- Alexandrova, O., Chen, C. H. K., Sorriso-Valvo, L., Horbury, T. S., & Bale, S. D. (2013). Solar wind turbulence and the role of ion instabilities. *Space Science Reviews*, *178*, 25–63. [https://doi.org/10.1007/978-1-4899-7413-6\\_3](https://doi.org/10.1007/978-1-4899-7413-6_3)
- Alexandrova, O., Jagarlamudi, V. K., Maksimovic, M., Hellinger, P., Shprits, Y., & Mangeney, A. (2021). Spectrum of kinetic plasma turbulence at 0.3–0.9 astronomical units from the Sun. *Physical Review E - Statistical Physics, Plasmas, Fluids, and Related Interdisciplinary Topics*, *103*(6), 063202. <https://doi.org/10.1103/PhysRevE.103.063202>
- Alexandrova, O., Jagarlamudi, V. K., Rossi, C., Maksimovic, M., Hellinger, P., Shprits, Y., & Mangeney, A. (2020). Kinetic turbulence in space plasmas observed in the near-Earth and near-Sun solar wind (Vol. 1–12).
- Alexandrova, O., Lacombe, C., & Mangeney, A. (2008). Spectra and anisotropy of magnetic fluctuations in the Earth's magnetosheath: Cluster observations. *Annales Geophysicae*, *26*(11), 3585–3596. <https://doi.org/10.5194/angeo-26-3585-2008>
- Alexandrova, O., Lacombe, C., Mangeney, A., Grappin, R., & Maksimovic, M. (2012). Solar wind turbulent spectrum at plasma kinetic scales. *The Astrophysical Journal*, *760*(2), 121. <https://doi.org/10.1088/0004-637X/760/2/121>
- Alexandrova, O., Mangeney, A., Maksimovic, M., Cornilleau-Wehrin, N., Bosqued, J.-M., & André, M. (2006). Alfvén vortex filaments observed in magnetosheath downstream of a quasi-perpendicular bow shock. *Journal of Geophysical Research*, *111*(A12), A12208. <https://doi.org/10.1029/2006JA011934>
- Alexandrova, O., Mangeney, A., Maksimovic, M., Lacombe, C., Cornilleau-Wehrin, N., Lucek, E. A., & Fazakerley, A. N. (2004). Cluster observations of finite amplitude Alfvén waves and small-scale magnetic filaments downstream of a quasi-perpendicular shock. *Journal of Geophysical Research*, *109*(A5), 1–12. <https://doi.org/10.1029/2003JA010056>
- Alexandrova, O., & Saur, J. (2008). Alfvén vortices in Saturn's magnetosheath: Cassini observations. *Geophysical Research Letters*, *35*(15), L15102. <https://doi.org/10.1029/2008GL034411>
- Alexandrova, O., Saur, J., Lacombe, C., Mangeney, A., Mitchell, J., Schwartz, S., & Robert, P. (2009). Universality of solar-wind turbulent spectrum from MHD to electron scales. *Physical Review Letters*, *103*(165003). <https://doi.org/10.1103/PhysRevLett.103.165003>
- Alexandrova, O., Saur, J., Lacombe, C., Mangeney, A., Schwartz, S. J., Mitchell, J., et al. (2010). Solar wind turbulent spectrum from MHD to electron scales. *AIP Conference Proceedings*, *1216*, 144–147. <https://doi.org/10.1063/1.3395821>
- Argall, M. R., Fischer, D., Le Contel, O., Mirioni, L., Torbert, R. B., Dors, I., et al. (2018). The fluxgate-searchcoil merged (FSM) magnetic field data product for MMS.
- Balogh, A., Carr, C., Acuña, M. H., Dunlop, M. W., Beek, T. J., Brown, P., et al. (2001). The cluster magnetic field investigation: Overview of in-flight performance and initial results. *Annales Geophysicae*, *19*(10/12), 1207–1217. <https://doi.org/10.5194/angeo-19-1207-2001>
- Bandyopadhyay, R., Chasapis, A., Chhiber, R., Parashar, T. N., Maruca, B. A., Matthaeus, W. H., et al. (2018). Solar wind turbulence studies using MMS fast plasma investigation data. *The Astrophysical Journal*, *866*(2), 81. <https://doi.org/10.3847/1538-4357/aade93>
- Bieber, J. W., Chen, J., Matthaeus, W. H., Smith, C. W., & Pomerantz, M. (1993). Long-term variations of interplanetary magnetic field spectra with implications for cosmic ray modulation. *Journal of Geophysical Research*, *98*(A3), 3585–3603. <https://doi.org/10.1029/92JA02566>
- Bieber, J. W., Wanner, W., & Matthaeus, W. H. (1996). Dominant two-dimensional solar wind turbulence with implications for cosmic ray transport. *Journal of Geophysical Research*, *101*(A2), 2511–2522. <https://doi.org/10.1029/95JA02588>
- Boldyrev, S. (2006). Spectrum of magnetohydrodynamic turbulence. *Physical Review Letters*, *96*(115002), 1–4. <https://doi.org/10.1103/PhysRevLett.96.115002>
- Borovsky, J. E., & Podesta, J. J. (2015). Exploring the effect of current sheet thickness on the high-frequency Fourier spectrum breakpoint of the solar wind. *Journal of Geophysical Research: Space Physics*, *120*(11), 9256–9268. <https://doi.org/10.1002/2015JA021622>
- Bowen, T. A., Bale, S. D., Bandyopadhyay, R., Bonnell, J. W., Case, A., Chasapis, A., et al. (2021). Kinetic-scale turbulence in the Venusian magnetosheath. *Geophysical Research Letters*, *48*(2), e2020GL090783. <https://doi.org/10.1029/2020GL090783>
- Bowen, T. A., Bale, S. D., Bonnell, J. W., Dudok de Wit, T., Goetz, K., Goodrich, K., et al. (2020). A merged search-coil and fluxgate magnetometer data product for parker solar probe FIELDS. *Journal of Geophysical Research: Space Physics*, *125*(5), e2020JA027813. <https://doi.org/10.1029/2020JA027813>
- Bruno, R. (2019). Intermittency in solar wind turbulence from fluid to kinetic scales. *Earth and Space Science*, *6*(5), 656–672. <https://doi.org/10.1029/2018EA000535>
- Bruno, R., & Carbone, V. (2013). The solar wind as a turbulence laboratory. *Living Reviews in Solar Physics*, *10*(2). <https://doi.org/10.12942/lrsp-2013-2>
- Bruno, R., Carbone, V., Primavera, L., Malara, F., Sorriso-Valvo, L., Bavassano, B., & Veltri, P. (2004). On the probability distribution function of small-scale interplanetary magnetic field fluctuations. *Annales Geophysicae*, *22*(10), 3751–3769. <https://doi.org/10.5194/angeo-22-3751-2004>
- Bruno, R., Carbone, V., Sorriso-Valvo, L., & Bavassano, B. (2003). Radial evolution of solar wind intermittency in the inner heliosphere. *Journal of Geophysical Research*, *108*(A3), 1–15. <https://doi.org/10.1029/2002JA009615>
- Bruno, R., Telloni, D., Primavera, L., Pietropaolo, E., D'Amicis, R., Sorriso-Valvo, L., et al. (2014). Radial evolution of the intermittency of density fluctuations in the fast solar wind. *The Astrophysical Journal*, *786*(1), 53. <https://doi.org/10.1088/0004-637X/786/1/53>
- Bruno, R., & Trenchi, L. (2014). Radial dependence of the frequency break between fluid and kinetic scales in the solar wind fluctuations. *The Astrophysical Journal*, *787*(2), L24. <https://doi.org/10.1088/2041-8205/787/2/L24>
- Carbone, F., Sorriso-Valvo, L., Alberti, T., Lepreti, F., Chen, C. H. K., Němeček, Z., & Šafránková, J. (2018). Arbitrary-order Hilbert spectral analysis and intermittency in solar wind density fluctuations. *The Astrophysical Journal*, *859*(1), 27. <https://doi.org/10.3847/1538-4357/aabcc2>
- Carbone, F., Sorriso-Valvo, L., Khotyaintsev, Y. V., Steinvaill, K., Vecchio, A., Telloni, D., et al. (2021). Statistical study of electron density turbulence and ion-cyclotron waves in the inner heliosphere: Solar Orbiter observations.
- Cerri, S. S., Groslej, D., & Franci, L. (2019). Kinetic plasma turbulence: Recent insights and open questions from 3D3V simulations. *Frontiers in Astronomy and Space Sciences*, *6*. <https://doi.org/10.3389/fspas.2019.00064>
- Chandran, B. D., Schekochihin, A. A., & Mallet, A. (2015). Intermittency and alignment in strong RMHD turbulence. *The Astrophysical Journal*, *807*(1), 39. <https://doi.org/10.1088/0004-637X/807/1/39>
- Chapman, S. C., Hnat, B., & Kiyani, K. H. (2008). Solar cycle dependence of scaling in solar wind fluctuations. *Nonlinear Processes in Geophysics*, *15*(3), 445–455. <https://doi.org/10.5194/npg-15-445-2008>

- Chapman, S. C., Hnat, B., Rowlands, G., & Watkins, N. W. (2005). Scaling collapse and structure functions: Identifying self-affinity in finite length time series. *Nonlinear Processes in Geophysics*, 12(6), 767–774. <https://doi.org/10.5194/npg-12-767-2005>
- Chasapis, A., Matthaeus, W. H., Bandyopadhyay, R., Chhiber, R., Ahmadi, N., Ergun, R. E., et al. (2020). Scaling and anisotropy of solar wind turbulence at kinetic scales during the MMS turbulence campaign. *The Astrophysical Journal*, 903(2), 127. <https://doi.org/10.3847/1538-4357/abb948>
- Chasapis, A., Matthaeus, W. H., Parashar, T. N., Fuselier, S. A., Maruca, B. A., Phan, T. D., et al. (2017). High-resolution statistics of solar wind turbulence at kinetic scales using the magnetospheric multiscale mission. *The Astrophysical Journal*, 844(1), L9. <https://doi.org/10.3847/2041-8213/aa7ddd>
- Chasapis, A., Matthaeus, W. H., Parashar, T. N., LeContel, O., Retinò, A., Breuillard, H., et al. (2017). Electron heating at kinetic scales in magnetosheath turbulence. *The Astrophysical Journal*, 836(2), 247. <https://doi.org/10.3847/1538-4357/836/2/247>
- Chen, C. H. K., Horbury, T. S., Schekochihin, A. A., Wicks, R. T., Alexandrova, O., & Mitchell, J. (2010). Anisotropy of solar wind turbulence between ion and electron scales. *Physical Review Letters*, 104(255002), 1–4. <https://doi.org/10.1103/PhysRevLett.104.255002>
- Chen, C. H. K., Leung, L., Boldyrev, S., Maruca, B., & Bale, S. D. (2014). Ion-scale spectral break of solar wind turbulence at high and low beta. *Geophysical Research Letters*, 41(8081–8088), 8081–8088. <https://doi.org/10.1002/2014GL026009>
- Chen, C. H. K., Mallet, A., Schekochihin, A., Horbury, T., Wicks, R. T., & Bale, S. (2012). Three-dimensional structure of solar wind turbulence. *The Astrophysical Journal*, 758(120), 1–5. <https://doi.org/10.1088/0004-637X/758/2/120>
- Chen, C. H. K., Sorriso-Valvo, L., Šafránková, J., & Němeček, Z. (2014). Intermittency of solar wind density fluctuations from ion to electron scales. *The Astrophysical Journal*, 789(1), L8. <https://doi.org/10.1088/2041-8205/789/1/L8>
- Chen, C. H. K., Wicks, R. T., Horbury, T. S., & Schekochihin, A. A. (2010). Interpreting power anisotropy measurements in plasma turbulence. *The Astrophysical Journal*, 711(L79–L83), L79–L83. <https://doi.org/10.1088/2041-8205/711/2/L79>
- Chhiber, R., Chasapis, A., Bandyopadhyay, R., Parashar, T. N., Matthaeus, W. H., Maruca, B. A., et al. (2018). Higher-order turbulence statistics in the Earth's magnetosheath and the solar wind using magnetospheric multiscale Observations. *Journal of Geophysical Research: Space Physics*, 123(12), 9941–9954. <https://doi.org/10.1029/2018JA025768>
- Chhiber, R., Matthaeus, W. H., Bowen, T. A., & Bale, S. D. (2021). Subproton-scale intermittency in near-sun solar wind turbulence observed by the Parker solar probe. Retrieved from <http://arxiv.org/abs/2102.10181>
- Cho, J. (2019). A technique for removing large-scale variations in regularly and irregularly spaced data Jungyeon. *The Astrophysical Journal*, 874(75). <https://doi.org/10.3847/1538-4357/ab06f3>
- Cornilleau-Wehrin, N., Chanteur, G., Perraut, S., Rezeau, L., Robert, P., Roux, A., et al. (2003). First results obtained by the Cluster STAFF experiment. *Annales Geophysicae*, 21(2), 437–456. <https://doi.org/10.5194/angeo-21-437-2003>
- Cornilleau-Wehrin, N., Chauveau, P., Louis, S., Meyer, A., Nappa, J. M., Perraut, S., et al. (1997). The cluster spatio-temporal analysis of field fluctuations (STAFF) experiment. *Space Science Reviews*.
- Dai, L., Wang, C., Cai, Z., Gonzalez, W., Hesse, M., Escoubet, P., et al. (2020). AME: A cross-scale constellation of cubesats to explore magnetic reconnection in the solar–terrestrial relation. *Frontiers in Physics*, 8(April), 1–14. <https://doi.org/10.3389/fphy.2020.00089>
- D'Amicis, R., Matteini, L., & Bruno, R. (2018). On slow solar wind with high Alfvénicity: From composition and microphysics to spectral properties. *Monthly Notices of the Royal Astronomical Society*, 483(4), 4665–4677. <https://doi.org/10.1093/mnras/sty3329>
- Duan, D., Bowen, T., Chen, C. H. K., Mallet, A., He, J., Bale, S., et al. (2020). The radial dependence of proton-scale magnetic spectral break in slow solar wind during PSP encounter 2. *Astrophysical Journal Supplement*, (55), 246. <https://doi.org/10.3847/1538-4365/ab672d>
- Dudok de Wit, T. (2004). Can high-order moments be meaningfully estimated from experimental turbulence measurements? *Physical Review*, 70(5), 055302. <https://doi.org/10.1103/PhysRevE.70.055302>
- Dudok De Wit, T., Alexandrova, O., Furno, I., Sorriso-Valvo, L., & Zimbardo, G. (2013). Methods for characterising microphysical processes in plasmas. *Space Science Reviews*, 178(2–4), 665–693. <https://doi.org/10.1007/s11214-013-9974-9>
- Escoubet, C. P., Fehringer, M., & Goldstein, M. (2001). Introduction the cluster mission. *Annales Geophysicae*, 19(10/12), 1197–1200. <https://doi.org/10.5194/angeo-19-1197-2001>
- Escoubet, C. P., Schmidt, R., & Goldstein, M. (1997). Cluster – Science and mission overview. *Space Science Reviews*, 79(1–2), 11–32. <https://doi.org/10.1023/a:1004923124586>
- Fischer, D., Magnes, W., Hagen, C., Dors, I., Chutter, M. W., Needell, J., et al. (2016). Optimized merging of search coil and fluxgate data for MMS. *Geoscientific Instrumentation, Methods and Data Systems*, 5(2), 521–530. <https://doi.org/10.5194/gi-5-521-2016>
- Franci, L., Cerri, S. S., Califano, F., Landi, S., Papini, E., Verdini, A., et al. (2017). Magnetic reconnection as a driver for a sub-ion-scale cascade in plasma turbulence. *The Astrophysical Journal*, 850(1), L16. <https://doi.org/10.3847/2041-8213/aa93fb>
- Frisch, U. (1995). *Turbulence: The legacy of A. N. Kolmogorov*. Cambridge University Press.
- Génot, V. (2008). Mirror and firehose instabilities in the heliosheath. *The Astrophysical Journal Letters*, 687(2), 119–122. <https://doi.org/10.1086/593325>
- Génot, V., Budnik, E., Hellinger, P., Passot, T., Belmont, G., Trávníček, P. M., et al. (2009). Mirror structures above and below the linear instability threshold: Cluster observations, fluid model and hybrid simulations. *Annales Geophysicae*, 27(2), 601–615. <https://doi.org/10.5194/angeo-27-601-2009>
- Hada, T., Koga, D., & Yamamoto, E. (2003). Phase coherence of MHD waves in the solar wind. *Space Science Reviews*, 107(1–2), 463–466. <https://doi.org/10.1023/A:1025506124402>
- Hadid, L., Sahaouhi, F., Kiyami, K. H., Retino, A., Modolo, R., Canu, P., et al. (2015). Nature of the MHD and kinetic scale turbulence in the magnetosheath of Saturn: Cassini observations. *The Astrophysical Journal Letters*, 813, L29. <https://doi.org/10.1088/2041-8205/813/2/L29>
- Haynes, C. T., Burgess, D., Camporeale, E., & Sundberg, T. (2015). Electron vortex magnetic holes: A nonlinear coherent plasma structure. *Physics of Plasmas*, 22(1), 012309. <https://doi.org/10.1063/1.4906356>
- He, J., Marsch, E., Tu, C.-Y., Yao, S., & Tian, H. (2011). Possible evidence of Alfvén-cyclotron waves in the angle distribution of magnetic helicity of solar wind turbulence. *The Astrophysical Journal*, 731(2), 85. <https://doi.org/10.1088/0004-637X/731/2/85>
- Hellinger, P., Travnicek, P., Kasper, J. C., & Lazarus, A. J. (2006). Solar wind proton temperature anisotropy: Linear theory and WIND/SWE observations. *Geophysical Research Letters*, 33(9), 2–5. <https://doi.org/10.1029/2006GL025925>
- Hellinger, P., & Travnicek, P. M. (2008). Oblique proton fire hose instability in the expanding solar wind: Hybrid simulations. *Journal of Geophysical Research*, A10109(113), 503–506. <https://doi.org/10.1029/2008JA013416>
- Horbury, T., Foreman, M., & Oughton, S. (2008). Anisotropic scaling of magnetohydrodynamic turbulence. *Physical Review Letters*, 101(175005), 1–4. <https://doi.org/10.1103/PhysRevLett.101.175005>
- Horbury, T., Forman, M. a., & Oughton, S. (2005). Spacecraft observations of solar wind turbulence: An overview. *Plasma Physics and Controlled Fusion*, 47(12B), B703–B717. <https://doi.org/10.1088/0741-3335/47/12B/S52>

- Hospodarsky, G. B. (2016). Spaced-based search coil magnetometers. *Journal of Geophysical Research: Space Physics*, 121(12), 12068–12079. <https://doi.org/10.1002/2016JA022565>
- Howes, G. G., Klein, K. G., & TenBarge, J. M. (2014). Validity of the Taylor hypothesis for linear kinetic waves in the weakly collisional solar wind. *The Astrophysical Journal*, 789(2), 106. <https://doi.org/10.1088/0004-637X/789/2/106>
- Huang, S. Y., Xiong, Q. Y., Yuan, Z. G., Zhan, H. L., Deng, X. H., Jiang, K., et al. (2021). Multi-spacecraft measurement of anisotropic spatial correlation functions at kinetic range in the magnetosheath turbulence. *Journal of Geophysical Research: Space Physics*, 126(5), e2020JA028780. <https://doi.org/10.1029/2020JA028780>
- Huang, Y. X., Schmitt, F. G., Lu, Z. M., Fougairrolles, P., Gagne, Y., & Liu, Y. L. (2021). Second order structure function in fully developed turbulence. *Physical Review E - Statistical, Nonlinear and Soft Matter Physics*, 82(2), 026319. <https://doi.org/10.1103/PhysRevE.82.026319>
- Jagarlamudi, V. K., Alexandrova, O., Berčić, L., de Wit, T. D., Krasnoselskikh, V., Maksimovic, M., & Štverák, Š. (2020). Whistler waves and electron properties in the inner heliosphere: Helios observations. *The Astrophysical Journal*, 897(2), 118. <https://doi.org/10.3847/1538-4357/ab94a1>
- Jagarlamudi, V. K., Dudok de Wit, T., Krasnoselskikh, V., & Maksimovic, M. (2019). Inherentness of non-stationarity in solar wind. *The Astrophysical Journal*, 871(1), 68. <https://doi.org/10.3847/1538-4357/aaef2e>
- Johnstone, A. D., Alsop, C., Burge, S., Carter, P. J., Coates, A. J., Coker, A. J., et al. (1997). PEACE: A plasma electron and current experiment. *Space Science Reviews*, 79(1/2), 351–398. <https://doi.org/10.1023/a:1004938001388>
- Jovanović, D., Alexandrova, O., & Maksimović, M. (2015). Theory of coherent electron-scale magnetic structures in space plasma turbulence. *Physica Scripta*, 90(8), 088002. <https://doi.org/10.1088/0031-8949/90/8/088002>
- Jovanović, D., Alexandrova, O., Maksimović, M., & Belić, M. (2020). Fluid theory of coherent magnetic vortices in high- $\beta$  space plasmas. *The Astrophysical Journal*, 896(8). <https://doi.org/10.3847/1538-4357/ab8a45>
- Kholyaintsev, Y. V., Graham, D. B., Norgren, C., & Vaivads, A. (2019). Collisionless magnetic reconnection and waves: Progress review. *Frontiers in Astronomy and Space Sciences*, 6(November), 1–20. <https://doi.org/10.3389/fspas.2019.00070>
- King, J. H., & Papitashvili, N. (2005). Solar wind spatial scales in and comparisons of hourly wind and ACE plasma and magnetic field data. *Journal of Geophysical Research*, 110(A2), A02104. <https://doi.org/10.1029/2004JA010649>
- Kiyani, K. H., Chapman, S. C., & Hnat, B. (2006). Extracting the scaling exponents of a self-affine, non-Gaussian process from a finite-length time series. *Physical Review*, 74(5), 051122. <https://doi.org/10.1103/PhysRevE.74.051122>
- Kiyani, K. H., Chapman, S. C., Kholyaintsev, Y. V., Dunlop, M. W., & Sahraoui, F. (2009). Global scale-invariant dissipation in collisionless plasma turbulence. *Physical Review Letters*, 103(7), 075006. <https://doi.org/10.1103/PhysRevLett.103.075006>
- Kiyani, K. H., Chapman, S. C., Sahraoui, F., Hnat, B., Fauvarque, O., & Kholyaintsev, Y. V. (2013). Enhanced magnetic compressibility and isotropic scale invariance at sub-ion Larmor scales in solar wind turbulence. *The Astrophysical Journal*, 763(1), 10. <https://doi.org/10.1088/0004-637X/763/1/10>
- Kiyani, K. H., Osman, K. T., & Chapman, S. C. (2015). Dissipation and heating in solar wind turbulence: From the macro to the micro and back again. *Philosophical Transactions of the Royal Society A: Mathematical, Physical & Engineering Sciences*, 373(2041), 20140155. <https://doi.org/10.1098/rsta.2014.0155>
- Klein, K. G., Alexandrova, O., Bookbinder, J., Caprioli, D., Case, A. W., Chandran, B. D. G., et al. (2019). [Plasma 2020 decadal] multipoint measurements of the solar wind: A proposed advance for studying magnetized turbulence. Retrieved from <http://arxiv.org/abs/1903.05740>
- Klein, K. G., Alterman, B. L., Stevens, M. L., Vech, D., & Kasper, J. C. (2018). Majority of solar wind intervals support ion-driven instabilities. *Physical Review Letters*, 120(20), 205102. <https://doi.org/10.1103/PhysRevLett.120.205102>
- Klein, K. G., Howes, G. G., & TenBarge, J. M. (2014). The violation of the Taylor hypothesis in measurements of solar wind turbulence. *The Astrophysical Journal*, 790(2), L20. <https://doi.org/10.1088/2041-8205/790/2/L20>
- Koga, D., & Hada, T. (2003). Phase coherence of foreshock MHD waves: Wavelet analysis. *Space Science Reviews*, 107(1–2), 495–498. <https://doi.org/10.1023/A:1025510225311>
- Kolmogorov, A. N. (1962). A refinement of previous hypotheses concerning the local structure of turbulence in a viscous incompressible fluid at high Reynolds number. *Journal of Fluid Mechanics*, 13(1), 82–85. <https://doi.org/10.1017/S0022112062000518>
- Laakso, H., Perry, C., McCaffrey, S., Herment, D., Allen, A. J., Harvey, C. C., et al. (2010). Cluster active archive: Overview. In (pp. 3–37). [https://doi.org/10.1007/978-90-481-3499-1\\_1](https://doi.org/10.1007/978-90-481-3499-1_1)
- Lacombe, C., Alexandrova, O., & Matteini, L. (2017). Anisotropies of the magnetic field fluctuations at kinetic scales in the solar wind: Cluster observations. *The Astrophysical Journal*, 848(45). <https://doi.org/10.3847/1538-4357/aa8c06>
- Lacombe, C., Alexandrova, O., Matteini, L., Santolík, O., Cornilleau-Wehrlin, N., Mangeney, A., et al. (2014). Whistler mode waves and the electron heat flux in the solar wind: Cluster observations. *The Astrophysical Journal*, 796(1), 5. <https://doi.org/10.1088/0004-637X/796/1/5>
- Landi, S., Franci, L., Papini, E., Verdini, A., Matteini, L., & Hellinger, P. (2019). Spectral anisotropies and intermittency of plasma turbulence at ion kinetic scales.
- Leamon, R. J., Smith, C. W., Ness, N. F., Matthaeus, W. H., & Wong, H. K. (1998). Observational constraints on the dynamics of the interplanetary magnetic field dissipation range. *Journal of Geophysical Research*, 103(A3), 4775–4787. <https://doi.org/10.1029/97ja03394>
- Lion, S., Alexandrova, O., & Zaslavsky, A. (2016). Coherent events and spectral shape at ion kinetic scales in the fast solar wind turbulence. *The Astrophysical Journal*, 824(1), 47. <https://doi.org/10.3847/0004-637X/824/1/47>
- Macek, W. M. (2007). Multifractality and intermittency in the solar wind. *Nonlinear Processes in Geophysics*, 14(6), 695–700. <https://doi.org/10.5194/npg-14-695-2007>
- Macek, W. M., Wawrzaszek, A., & Carbone, V. (2011). Observation of the multifractal spectrum at the termination shock by Voyager 1. *Geophysical Research Letters*, 38(19), 1–5. <https://doi.org/10.1029/2011GL049261>
- Mallet, A., Klein, K. G., Chandran, B. D. G., Grošelj, D., Hoppock, I. W., Bowen, T. A., et al. (2019). Interplay between intermittency and dissipation in collisionless plasma turbulence. *Journal of Plasma Physics*, 85(3), 175850302. <https://doi.org/10.1017/S0022377819000357>
- Mallet, A., Schekochihin, A. A., & Chandran, B. (2011). Disruption of sheet-like structures in Alfvénic turbulence by magnetic reconnection. *MNRAS*, 468(4), 4862–4871. <https://doi.org/10.1093/mnras/stx670>
- Mangeney, A., Lacombe, C., Maksimovic, M., Samsonov, A. A., Cornilleau-Wehrlin, N., Harvey, C. C., et al. (2006). Cluster observations in the magnetosheath – Part I: Anisotropies of the wave vector distribution of the turbulence at electron scales. *Annales Geophysicae*, 24(12), 3507–3521. <https://doi.org/10.5194/angeo-24-3507-2006>
- Mangeney, A., Salem, C., Veltri, P. L., & Cecconi, B. (2001). *Intermittency in the solar wind turbulence and the Haar wavelet transform* (pp. 53–64). European Space Agency, (Special Publication) ESA SP.
- Matteini, L., Franci, L., Alexandrova, O., Lacombe, C., Landi, S., Hellinger, P., et al. (2020). Magnetic field turbulence in the solar wind at sub-ion scales: In situ observations and numerical simulations. *Frontiers in Astronomy and Space Sciences*, 7, 1–20. <https://doi.org/10.3389/fspas.2020.563075>

- Matthaeus, W. H., Bandyopadhyay, R., Brown, M. R., Borovsky, J., Carbone, V., Caprioli, D., et al. (2019). [Plasma2020 Decadal] the essential role of multi-point measurements in turbulence investigations: The solar wind beyond single scale and beyond the Taylor Hypothesis. Retrieved from <http://arxiv.org/abs/1903.06890>
- Matthaeus, W. H., Wan, M., Servidio, S., Greco, A., Osman, K. T., Oughton, S., & Dmitruk, P. (2015). Intermittency, nonlinear dynamics and dissipation in the solar wind and astrophysical plasmas. *Philosophical Transactions of the Royal Society A: Mathematical, Physical & Engineering Sciences*, 373(20140154). <https://doi.org/10.1098/rsta.2014.0154>
- Monin, A. S., Yaglom, A. M., & Lumley, J. L. (1975). *Statistical fluid mechanics* (Vol. 2). MIT Press.
- Montgomery, D. (1980). *Report of the NASA plasma turbulence explorer study group (Tech. Rep.)*. NASA, Jet Propulsion Laboratory.
- Narita, Y., Gary, S. P., Saito, S., Glassmeier, K.-H., & Motschmann, U. (2011). Dispersion relation analysis of solar wind turbulence. *Geophysical Research Letters*, 38, L05101. <https://doi.org/10.1029/2010GL046588>
- Osman, K., Matthaeus, W., Greco, A., & Servidio, S. (2011). Evidence for inhomogeneous heating in the solar wind. *The Astrophysical Journal*, 727(1), L11. <https://doi.org/10.1088/2041-8205/727/1/L11>
- Oughton, S., Matthaeus, W., Wan, M., & Osman, K. T. (2015). Anisotropy in solar wind plasma turbulence. *Philosophical Transactions of the Royal Society A: Mathematical, Physical & Engineering Sciences*, 373(2041), 20140152. <https://doi.org/10.1098/rsta.2014.0152>
- Oughton, S., & Matthaeus, W. H. (2020). Critical balance and the physics of magnetohydrodynamic turbulence. *The Astrophysical Journal*, 897(1), 37. <https://doi.org/10.3847/1538-4357/ab8f2a>
- Perri, S., Carbone, V., Vecchio, A., Bruno, R., Korth, H., Zurbuchen, T. H., & Sorriso-Valvo, L. (2012). Phase-synchronization, energy cascade, and intermittency in solar-wind turbulence. *Physical Review Letters*, 109(24), 245004. <https://doi.org/10.1103/PhysRevLett.109.245004>
- Perri, S., Goldstein, M., Dorelli, J., & Sahraoui, F. (2012). Detection of small-scale structures in the dissipation regime of solar-wind turbulence. *Physical Review Letters*, 109(19), 191101. <https://doi.org/10.1103/PhysRevLett.109.191101>
- Perri, S., Servidio, S., Vaivads, A., & Valentini, F. (2017). Numerical study on the validity of the Taylor hypothesis in space plasmas. *The Astrophysical Journal - Supplement Series*, 231(1), 4. <https://doi.org/10.3847/1538-4365/aa755a>
- Perri, Y., Yordanova, E., Carbone, V., Veltri, P., Sorriso-Valvo, L., Bruno, R., & Andre, M. (2009). Magnetic turbulence in space plasmas: Scale-dependent effects of anisotropy. *Journal of Geophysical Research*, 114(A2), A02102. <https://doi.org/10.1029/2008JA013491>
- Perrone, D., Alexandrova, O., Mangeny, A., Maksimovic, M., Lacombe, C., Rakoto, J., et al. (2016). Compressive coherent structures at ion scales in the slow solar wind. *The Astrophysical Journal*, 826(2), 196. <https://doi.org/10.3847/0004-637X/826/2/196>
- Perrone, D., Alexandrova, O., Roberts, O. W., Lion, S., Lacombe, C., Walsh, A., et al. (2017). Coherent structures at ion scales in fast solar wind: Cluster observations. *The Astrophysical Journal*, 849(1), 49. <https://doi.org/10.3847/1538-4357/aa9022>
- Phan, T. D., Eastwood, J. P., Shay, M. A., Drake, J. F., Sonnerup, B. U., Fujimoto, M., et al. (2018). Electron magnetic reconnection without ion coupling in Earth's turbulent magnetosheath. *Nature*, 557(7704), 202–206. <https://doi.org/10.1038/s41586-018-0091-5>
- Quijia, P., Fraternali, F., Stawarz, J., Vásconez, C., Perri, S., Marino, R., et al. (2021). Comparing turbulence in a Kelvin–Helmholtz instability region across the terrestrial magnetopause. *MNRAS*, 503(4), 4815–4842. <https://doi.org/10.1093/mnras/stab319>
- Reme, H., Aoustin, C., Bosqued, J. M., Dandouras, I., Lavraud, B., Sauvaud, J. A., et al. (2001). First multispacecraft ion measurements in and near the Earth's magnetosphere with the identical cluster ion spectrometry (CIS) experiment. *Annales Geophysicae*, 19(10/12), 1303–1354. <https://doi.org/10.5194/angeo-19-1303-2001>
- Reme, H., Bosqued, J., & Sauvaud, J. (1997). The cluster ion spectrometry (CIS) experiment. *Space Science Reviews*, 303–350. Retrieved from [http://link.springer.com/chapter/10.1007/978-94-011-5666-0/\\_12](http://link.springer.com/chapter/10.1007/978-94-011-5666-0/_12)
- Robert, P., Cornilleau-Wehrlin, N., Piberne, R., de Conchy, Y., Lacombe, C., Bouzid, V., et al. (2014). Cluster–staff search coil magnetometer calibration – Comparisons with FGM. *Geoscientific Instrumentation. Methods and Data Systems*, 3(2), 153–177. <https://doi.org/10.5194/gi-3-153-2014>
- Roberts, O. W., Alexandrova, O., Kajdič, P., Turc, L., Perrone, D., Escoubet, C. P., & Walsh, A. (2017). Variability of the magnetic field power spectrum in the solar wind at electron scales. *The Astrophysical Journal*, 850(2), 120. <https://doi.org/10.3847/1538-4357/aa93e5>
- Roberts, O. W., Li, X., Alexandrova, O., & Li, B. (2016). Observation of an MHD Alfvén vortex in the slow solar wind. *Journal of Geophysical Research: Space Physics*, 121(5), 3870–3881. <https://doi.org/10.1002/2015JA022248>
- Roberts, O. W., Li, X., & Li, B. (2013). Kinetic plasma turbulence in the fast solar wind measured by cluster. *The Astrophysical Journal*, 769(58). <https://doi.org/10.1088/0004-637X/769/1/58>
- Roberts, O. W., Thwaites, J., Sorriso-Valvo, L., Nakamura, R., & Vörös, Z. (2020). Higher-order statistics in compressive solar wind plasma turbulence: High-resolution density observations from the magnetospheric multiscale mission. *Frontiers in Physics*, 8(October), 1–14. <https://doi.org/10.3389/fphy.2020.584063>
- Roberts, O. W., Verscharen, D., Narita, Y., Nakamura, R., Vörös, Z., & Plaschke, F. (2020). Possible coexistence of kinetic Alfvén and ion Bernstein modes in sub-ion scale compressive turbulence in the solar wind. *Physical Review Research*, 2(4), 43253. <https://doi.org/10.1103/PhysRevResearch.2.043253>
- Sahraoui, F., Goldstein, M., Belmont, G., Canu, P., & Rezeau, L. (2010). Three dimensional anisotropic k spectra of turbulence at subproton scales in the solar wind. *Physical Review Letters*, 105(131101). <https://doi.org/10.1103/PhysRevLett.105.131101>
- Sahraoui, F., Hadid, L., & Huang, S. (2020). Magnetohydrodynamic and kinetic scale turbulence in the near-Earth space plasmas: A (short) biased review. *Springer Singapore*, 4(No. 1). <https://doi.org/10.1007/s41614-020-0040-2>
- Sahraoui, F., Huang, S. Y., Belmont, G., Goldstein, M. L., Réтино, A., Robert, P., & De Patoul, J. (2013). Scaling of the electron dissipation range of solar wind turbulence. *The Astrophysical Journal*, 777(1), 15. <https://doi.org/10.1088/0004-637X/777/1/15>
- Salem, C., Mangeny, A., Bale, S. D., & Veltri, P. (2009). Solar wind magnetohydrodynamics turbulence: Anomalous scaling and role of intermittency. *The Astrophysical Journal*, 702(1), 537–553. <https://doi.org/10.1088/0004-637X/702/1/537>
- Saur, J., & Bieber, J. W. (1999). Geometry of low-frequency solar wind magnetic turbulence: Evidence for radially aligned Alfvénic fluctuations. *Journal of Geophysical Research*, 104(A5), 9975–9988. <https://doi.org/10.1029/1998JA900077>
- Schaffner, D. A., & Brown, M. R. (2015). Multifractal and monofractal scaling in a laboratory magnetohydrodynamic turbulence experiment. *The Astrophysical Journal*, 811(62), 61. <https://doi.org/10.1088/0004-637X/811/1/61>
- Schreiner, A., & Saur, J. (2017). A Model for dissipation of solar wind magnetic turbulence by kinetic Alfvén waves at electron scales: Comparison with observations. *The Astrophysical Journal*, 835(2), 133. <https://doi.org/10.3847/1538-4357/835/2/133>
- Schwartz, S. J., Hellinger, P., Bale, S., Owen, C., Nakamura, R., Vaivads, A., et al. (2011). Preface: Cross-scale coupling in plasmas. *Planetary and Space Science*, 59(7), 447–448. <https://doi.org/10.1016/j.pss.2011.02.006>
- Sorriso-Valvo, L., Carbone, F., Leonardis, E., Chen, C. H. K., Šafránková, J., & Němeček, Z. (2017). Multifractal analysis of high resolution solar wind proton density measurements. *Advances in Space Research*, 59(6), 1642–1651. <https://doi.org/10.1016/j.asr.2016.12.024>
- Sorriso-Valvo, L., Carbone, F., Perri, S., Greco, A., Marino, R., & Bruno, R. (2018). On the statistical properties of turbulent energy transfer rate in the inner heliosphere. *Solar Physics*, 293(1), 1–10. <https://doi.org/10.1007/s11207-017-1229-6>

- Sorriso-Valvo, L., Carbone, V., Bruno, R., & Veltri, P. (2006). Persistence of small-scale anisotropy of magnetic turbulence as observed in the solar wind. *Europhysics Letters*, 75(5), 832–838. <https://doi.org/10.1209/epl/i2006-10172-y>
- Sorriso-Valvo, L., Carbone, V., Veltri, P., Consolini, G., & Bruno, R. (1999). Intermittency in the solar wind turbulence through probability distribution functions of fluctuations. *Geophysical Research Letters*, 26(13), 1801–1804. <https://doi.org/10.1029/1999GL900270>
- Sorriso-Valvo, L., Yordanova, E., & Carbone, V. (2010). On the scaling properties of anisotropy of interplanetary magnetic turbulent fluctuations. *EPL*, 90(5), 59001. <https://doi.org/10.1209/0295-5075/90/59001>
- Soucek, J., & Escoubet, C. P. (2011). Cluster observations of trapped ions interacting with magnetosheath mirror modes. *Annales Geophysicae*, 29(6), 1049–1060. <https://doi.org/10.5194/angeo-29-1049-2011>
- Soucek, J., Lucek, E., & Dandouras, I. (2008). Properties of magnetosheath mirror modes observed by Cluster and their response to changes in plasma parameters. *Journal of Geophysical Research*, 113(A4), A04203. <https://doi.org/10.1029/2007JA012649>
- Tao, C., Sahraoui, F., de Patoul, J., Chust, T., Kasahara, S., & Retino, A. (2015). Properties of Jupiter's magnetospheric turbulence observed by the Galileo spacecraft. *Journal of Geophysical Research Space Physics*, 120(4), 2477–2493. <https://doi.org/10.1002/2014JA020749>
- TenBarge, J., Podesta, J. J., Klein, K. G., & Howes, G. G. (2012). Interpreting magnetic variance anisotropy measurements in the solar wind. *The Astrophysical Journal*, 753(107). <https://doi.org/10.1088/0004-637X/753/2/107>
- Tennekes, H., & Wyngaard, J. C. (1972). The intermittent small-scale structure of turbulence: Data-processing hazards. *Journal of Fluid Mechanics*, 55(1), 93–103. <https://doi.org/10.1017/S0022112072001661>
- Teodorescu, E., Echim, M., & Voicu, G. (2021). A perspective on the scaling of magnetosheath turbulence and effects of bow shock properties. *The Astrophysical Journal*, 910(1), 66. <https://doi.org/10.3847/1538-4357/abe12d>
- Torrence, C., & Compo, G. P. (1998). A practical guide to wavelet analysis. *Bulletin of the American Meteorological Society*, 79(1), 61–78. [https://doi.org/10.1175/1520-0477\(1998\)079<0061:APGTWA>2.0.CO;2](https://doi.org/10.1175/1520-0477(1998)079<0061:APGTWA>2.0.CO;2)
- Turc, L., Roberts, O. W., Archer, M. O., Palmroth, M., Battarbee, M., Brito, T., et al. (2019). First observations of the disruption of the Earth's foreshock wave field during magnetic clouds. *Geophysical Research Letters*, 46(22), 12644–12653. <https://doi.org/10.1029/2019GL084437>
- Vaivads, A., Retinò, A., Soucek, J., Khotyaintsev, Y. V., Valentini, F., Escoubet, C. P., et al. (2016). Turbulence heating observeR – Satellite mission proposal. *Journal of Plasma Physics*, 82(05), 905820501. <https://doi.org/10.1017/S0022377816000775>
- Vech, D., Mallet, A., Klein, K. G., & Kasper, J. C. (2018). Magnetic reconnection may control the ion-scale spectral break of solar wind turbulence. *The Astrophysical Journal*, 855(2), L27. <https://doi.org/10.3847/2041-8213/aab351>
- Veltri, P. (1999). MHD turbulence in the solar wind: Self-similarity, intermittency and coherent structures. *Plasma Physics and Controlled Fusion*, 41(3A), 787–A795. <https://doi.org/10.1088/0741-3335/41/3a/071>
- Verscharen, D., Klein, K. G., & Maruca, B. A. (2019). The multi-scale nature of the solar wind. *Living Reviews in Solar Physics*, 16(1), 5. <https://doi.org/10.1007/s41116-019-0021-0>
- Verscharen, D., Wicks, R. T., Alexandrova, O., Bruno, R., Burgess, D., Chen, C. H. K., et al. (2021). A case for electron-astrophysics. *Experimental Astronomy*. <https://doi.org/10.1007/s10686-021-09761-5>
- Volwerk, M., Goetz, C., Plaschke, F., Karlsson, T., Heyner, D., & Anderson, B. (2020). On the magnetic characteristics of magnetic holes in the solar wind between Mercury and Venus. *Annales Geophysicae*, 38(1), 51–60. <https://doi.org/10.5194/angeo-38-51-2020>
- Volwerk, M., Mautner, D., Simon Wedlund, C., Goetz, C., Plaschke, F., Karlsson, T., et al. (2021). Statistical study of linear magnetic hole structures near Earth. *Annales Geophysicae*, 39, 239–253. <https://doi.org/10.5194/angeo-2020-38>
- von Papen, M., Saur, J., & Alexandrova, O. (2014). Turbulent magnetic field fluctuations in Saturn's magnetosphere. *Journal of Geophysical Research: Space Physics*, 119(4), 2797–2818. <https://doi.org/10.1002/2013JA019542>
- Vörös, Z., Yordanova, E., Echim, M. M., Consolini, G., & Narita, Y. (2016). Turbulence-generated proton-scale structures in the terrestrial magnetosheath. *The Astrophysical Journal Letters*, 819(1). <https://doi.org/10.3847/2041-8205/819/1/L15>
- Wang, T., Alexandrova, O., Perrone, D., Dunlop, M., Dong, X., Bingham, R., et al. (2019). Magnetospheric multiscale observation of kinetic signatures in the Alfvén Vortex. *The Astrophysical Journal*, 871(2), L22. <https://doi.org/10.3847/2041-8213/aaf60d>
- Wang, T., He, J., Alexandrova, O., Dunlop, M., & Perrone, D. (2020). Observational quantification of three-dimensional anisotropies and scalings of space plasma turbulence at kinetic scales. *The Astrophysical Journal*, 898(1), 91. <https://doi.org/10.3847/1538-4357/ab99ca>
- Wu, P., Perri, S., Osman, K., Wan, M., Matthaeus, W., Shay, M., et al. (2013). Intermittent heating in solar wind and kinetic simulations. *The Astrophysical Journal Letters*, 763(2), L30. <https://doi.org/10.1088/2041-8205/763/2/L30>
- Yearby, K. H., Walker, S. N., & Balikhin, M. A. (2013). Enhanced timing accuracy for cluster data. *Geoscientific Instrumentation, Methods and Data Systems*, 2(2), 323–328. <https://doi.org/10.5194/gi-2-323-2013>
- Yordanova, E., Perri, S., Sorriso-Valvo, L., & Carbone, V. (2015). Multipoint observation of anisotropy and intermittency in solar-wind turbulence. *EPL*, 110(1), 19001. <https://doi.org/10.1209/0295-5075/110/19001>
- Yordanova, E., Vörös, Z., Raptis, S., & Karlsson, T. (2020). Current sheet statistics in the magnetosheath. *Frontiers in Astronomy and Space Sciences*, 7(2). <https://doi.org/10.3389/fspas.2020.00002>
- Yordanova, E., Vörös, Z., Sorriso-Valvo, L., Dimmock, A., & Kilpua, E. (2021). A possible link between turbulence and plasma heating. *The Astrophysical Journal*, 921(65). <https://doi.org/10.3847/1538-4357/ac1942>
- Yordanova, E., Vörös, Z., Varsani, A., Graham, D. B., Norgren, C., Khotyaintsev, Y. V., et al. (2016). Electron scale structures and magnetic reconnection signatures in the turbulent magnetosheath. *Geophysical Research Letters*, 43(12), 5969–5978. <https://doi.org/10.1002/2016GL069191>
- Zhang, J., Huang, S. Y., He, J. S., Wang, T. Y., Yuan, Z. G., Deng, X. H., et al. (2022). Three-dimensional anisotropy and scaling properties of solar wind turbulence at kinetic scales in the inner heliosphere: Parker solar probe observations. *The Astrophysical Journal Letters*, 924(2), L21. <https://doi.org/10.3847/2041-8213/ac4027>